FY21 Laboratory Basic Science Program

M. S. Wei

Laboratory for Laser Energetics, University of Rochester

The Laboratory Basic Science (LBS) Program awarded 22 projects with a total allocation of 23 shot days for a full year schedule at the Omega Laser Facility in FY21. Due to the delays of five FY20 LBS projects into FY21 as a result of the COVID-19 pandemic-caused disruption in FY20, six FY21 LBS projects were subsequently delayed into FY22. A total of 231 target shots were conducted over 21 days for 21 LBS projects including five from the FY20 program and 16 from the FY21 program. These experiments were led by scientists from Lawrence Livermore National Laboratory (LLNL), Los Alamos National Laboratory (LANL), Lawrence Berkeley National Laboratory (LBNL), and LLE (see Table I).

During FY21, LLE issued a solicitation for LBS proposal for beam time in FY22. A total of 27 proposals were submitted, requesting a total of 36 Omega shot days, exceeding the available LBS allocation by 232%, showing strong interest and high demand of Omega facility time for basic high-energy-density (HED) science experiments from the National Nuclear Security Administration Inertial Confinement Fusion (NNSA ICF) laboratories and the Office of Science laboratories. An independent LBS Proposal Review Panel (PRP) consisting of ten subject-matter experts from university, national laboratories, and industry reviewed and ranked the proposals. Based on the LBS PRP's recommendation, 15 FY22 LBS proposals were selected and allocated a total of 15.5 shot days for experiments at the Omega Laser Facility in FY22, as shown in Table II. With the six carryovers from the FY21 LBS program (shown in Table I), a total of 22 shot days are allocated for LBS experiments in FY22. The LBS experiments conducted in FY21 are summarized here.

Table I: LBS projects with experiments conducted at the Omega Laser Facility in FY21, including five carryovers from the FY20 LBS Program. The blue shaded cells are the five projects from the FY20 program. The gray shaded cells are the FY21 LBS projects postponed with shots rescheduled in FY22.

Principal Investigator	Institution	Title
F. Coppari	LLNL	The Atomic Structure and Melting of New Solid and Superionic Water Ices at Multi-Megabar Pressures: Searching for Ice XIX
Z. L. Mohamed	LLE	Study of Gamma-Ray Products from Reactions Relevant to Big-Bang Nucleosynthesis
A. Pak/N. Lemos	LLNL	Proton Radiography of Target Normal Sheath Acceleration Fields in the Long-Pulse Regime
H. G. Rinderknecht	LLE	Measuring the Triton Breakup Reaction T(n,2n)D
J. R. Rygg/H. Poole	LLE	Optical and X-Ray Scattering Measurements of Dense Silicon
F. Albert	LLNL	X-Ray Radiography with Sources Driven by Laser Wakefield Acceleration
F. Coppari	LLNL	Melting, Polymorphism, and Kinetics of Crystallization of Superionic Ice
T. Döppner	LLNL	Developing Fresnel Diffractive Radiography for Mutual Diffusion Measurements
D. E. Fratanduono/M. Millot	LLNL	Investigating Giant Impacts on Rocky Planets with High-Pressure Melting and Shock Equation-of-State Measurements on Complex Silicates

Table I: LBS projects with experiments conducted at the Omega Laser Facility in FY21, including five carryovers from the FY20 LBS Program. The blue shaded cells are the five projects from the FY20 program. The gray shaded cells are the FY21 LBS projects postponed with shots rescheduled in FY22 (continued).

Principal Investigator	Institution	Title
N. Lemos	LLNL	Proton Radiography of a Hybrid Laser Wakefield Accelerator Driven by a Picosecond–Kilojoule-Class Laser
L. Masse/S. Khan	LLNL	Evidencing the Transition from Landau–Darrieus Instability to Ablative Richtmyer–Meshkov Using Low-Density Foam Targets on OMEGA EP
P. M. Nilson/S. X. Hu	LLE	Atomic Physics at Petapascal Pressures
J. L. Peebles	LLE	Comparison and Validation of Dynamic Magnetic-Field Diagnostics on Laser-Driven Coils and MIFEDS
S. Singh	LLNL	Determination of High-Pressure Phase Transformation Mechanisms at the Atomic Scale
V. Smalyuk/H. Sio	LLNL	Kelvin–Helmholtz Instability with a Magnetic Twist
C. Stoeckl	LLE	Development of New Experimental Platform LIANS on OMEGA EP for Deuteron and Triton-Induced Nuclear Reactions
G. Tabak	LLE	Extreme Physics of Hydrogen and Water in Planetary Interiors
W. Theobald	LLE	X-Ray Phase-Contrast Imaging of Imploding Strong Shock Waves
T. J. Weber/M. P. Valdivia	LANL	Understanding Collisional Interpenetration of Ion Species with Talbot–Lau Interferometry
S. Zhao/C. Stan	LBNL	Extreme Deformation of High-Entropy Alloys
H. Chen/M. Edwards	LLNL	Developing a Magnetic Mirror Trap for Laser-Produced Relativistic Electron–Positron
H. Chen	LLNL	Measuring Particle Transport in Turbulent Plasmas
L. Gao	PPPL	Investigation of Magnetic-Field Generation with Short-Pulse Laser-Powered Capacitor Coils
Y.-J. Kim	LLNL	Extreme Chemistry Inside the Icy Planets: Shock Compression of Precompressed Ammonia–Water Mixtures
H. G. Rinderknecht	LLE	A Plasma Rectifier for Extreme Magnetic Fields, Efficient Electron Acceleration, and Bright X-Ray Sources
A.B. Zylstra	LLNL	Big-Bang Nucleosynthesis Relevant to the Primordial ^{7}Li Problem

PPPL: Princeton Plasma Physics Laboratory.

Expanding Our Understanding of Warm Dense Water Ices

Principal Investigators: F. Coppari (LLNL)
Co-investigators: Y.-J. Kim, J. H. Eggert, and M. Millot (LLNL)

Water exhibits a complex polymorphism at high pressures and temperatures. Twenty different forms of ice have been found experimentally, and more have been predicted to become stable at pressure exceeding 400 GPa. In 2021, we were allocated two shot days (one from the previous year's LBS allocation, delayed because of COVID-19) on the OMEGA EP Laser, where we collected a total of 15 shots in the two campaigns. The goal of these experiments was to expand our understanding of the structural properties of water ices in the warm-dense-matter regime relevant to planetary interiors. This research built on the success of a previous work performed on the OMEGA 60 laser that led to the discovery of a new form of ice (Ice XVIII) with superionic properties.[1,2]

Table II: LBS Program approved target shots at the Omega Laser Facility in FY22.

Principal Investigator	Institution	Title
F. Albert	LLNL	High-Precision X-Ray Radiography Driven by Laser Wakefield Acceleration
G. Bruhaug	LLE	Relativistic THz-Matter Interactions
S. Clarke	LLNL	The Effect of Ni Concentration on Phase Transformation Dynamics in the Fe-Ni Binary System
G. W. Collins	LLE	Quantum States of Hydrogen: Toward a Superconducting Superfluid
A. Gleason	SLAC	Viscosity Measurements Using Tracer Particles
I. V. Igumenshchev	LLE	Formation of Dynamic Shells Using Foam Ball Targets
J. Jeet	LLNL	Cross-Calibrations of the DT γ-to-Neutron and D–^{3}He γ-to-Proton Branching Ratios Against the ^{12}C(n,n$'$)γ Reaction
A. Krygier	LLNL	The Strength of Fe and Fe-Si 16 wt% at the Conditions in Earth's Core
S. Malko	PPPL	Detailed Benchmarking of the Nernst Effect in a Magnetized HED Plasma
J. L. Peebles	LLE	Probing In-Flight Vacuum Magnetic-Field Compression on OMEGA
M. J. Rosenberg	LLE	Electron Energization in Colliding and Reconnecting Magnetized Plasmas
M. B. Schneider	LLNL	Using Isoelectronic Line Ratios to Measure Density in Nonlocal Thermodynamic Equilibrium Plasmas
R. Smith	LLNL	Measuring the Viscosity of Silicates at Lower-Mantle Conditions
C. Stoeckl	LLE	Development of New Experimental Platform LIANS on OMEGA EP for Deuteron and Triton-Induced Nuclear Reactions
G. Swadling	LLNL	Angular Momentum Transport in Disk-Jet Transitions

Two laser beams were used to compress a thin liquid water layer to different pressures and temperatures, and two additional beams were used to generate a quasi-monochromatic x-ray source that enabled us to collect x-ray diffraction patterns, revealing the crystalline structure of water ices at extreme conditions, using the powder x-ray diffraction image plate (PXRDIP) diagnostic.[3]

In addition to the challenges related to the scientific goals of this campaign (i.e., obtaining a diffraction signal off a low scattering material and accurately designing the target geometry and pulse shape to reach specific pressure/temperature conditions), we had to overcome technical difficulties related to the confinement of a thin liquid water layer for a sufficiently long time (at least one week, from filling to shot time). Accurate metrology of the target was done prior to and after filling (in Livermore) and prior to the shot (in Rochester)[4] to ensure that the target was still holding water at shot time. We obtained excellent data (Fig. 1), whose analysis is underway, and will allow us to elucidate the complex behavior of warm dense water ices at extreme conditions.

Developing Fresnel Diffractive–Refractive Radiography for Experimental Measurements of Mutual Diffusivity in Warm Dense Matter

Principal Investigators: T. Döppner (LLNL)
Co-investigators: L. Divol, A. Kemp, O. L. Landen, Y. Ping, and M. Schölmerich (LLNL); T. G. White and C. H. Allen (University of Nevada, Reno); M. Oliver (Central Laser Facility, UK); and W. Theobald (LLE)

The experimental measurement of concentration-driven diffusion between two species in warm dense matter (WDM) is important for benchmarking instability growth simulations in ICF experiments.[5] The scale length of this mutual diffusion is of the order of 1 μm, necessitating a diagnostic tool that can resolve density gradient changes with submicron resolution. For FY21, we had a full shot day on OMEGA (MutualDiffusivity-21A), where we refined our Fresnel diffractive–refractive radiography imaging platform by measuring dynamic density gradients in WDM material, improving our previous results from FY20.

The development of this platform has progressed from imaging cold wire targets to sampling driven dynamic WDM systems, looking at the interface of isochorically heated W and fluorinated CH (Fig. 2). Our preliminary analysis shows significant expansion

in the W wire and shocks launched into the CH that evolve over time. We had nine target shots over the course of our shot day, five of which used our monolithic target[6] on OMEGA's planar cryocart mounts.
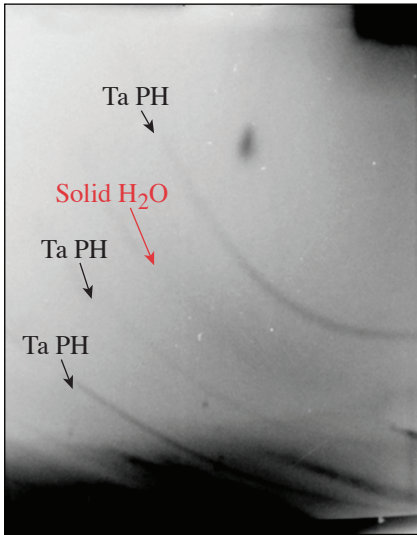
U2796JR

Figure 1
Example x-ray diffraction data. The red arrow points to the diffraction signal from water ice solidified by the laser-driven compression. Black arrows indicate diffraction signals from Ta at ambient conditions that allow us to accurately determine the geometry of the diffraction experiment.
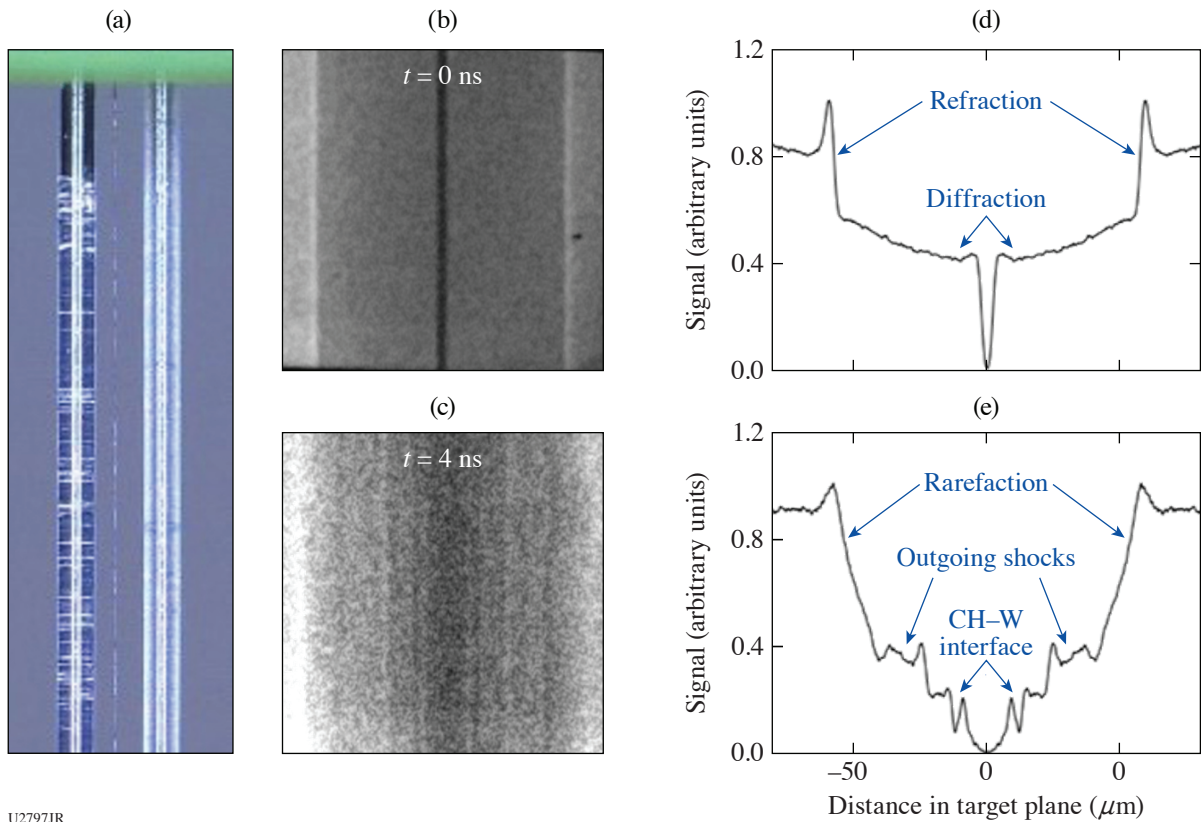
U2797JR

Figure 2
(a) Samples of our plastic-coated W wires alongside an uncoated W wire in between. These wires were coated via physical vapor deposition (PVD) at the Central Laser Facility (CLF), UK. [(b),(c)] Radiographs and [(d),(e)] lineouts of a cold target and a driven target, respectively. The clear change in the features is evident in the lineouts, showing the explosion of the W wire and the expanded CH–W interface as well as a shock wave launched into the CH.

Inelastic Reactions of $^{6(7)}$Li from 14-MeV Neutrons Using an Inertial Confinement Fusion Platform

Principal Investigators: C. J. Forrest, J. P. Knauer, P. B. Radha, V. Yu. Glebov, Z. L. Mohamed, S. P. Regan, and C. Stoeckl (LLE); and W. U. Schröder (LLE, Department of Chemistry and Physics, University of Rochester)

High-energy-density laboratory plasmas (HEDLP) is an established experimental platform that is used to address opportunities in a number of fields of scientific research.[7] Recently, HEDLP plasmas generated on the OMEGA laser[8] have been used to conduct basic nuclear science experiments. These facilities present viable and interesting alternatives to experimental accelerator-based platforms. In fact, primary yields are at the levels required to begin investigating fundamental nuclear reactions including neutron-induced breakup reactions of light nuclei. For these reasons, new fields of scientific exploration have been initiated for both nuclear interactions and high-energy-density plasmas.

The experimental campaign that was conducted in FY21 is part of an ongoing series of cross-section measurements using a platform for weapons-relevant, light-ion nuclear reaction experiments on OMEGA. A DT gas-filled implosion produces a point source of neutrons, and a heavily shielded neutron time-of-flight (nTOF) spectrometer measures the neutron spectrum from a sample along the line of sight to the detector. Four targets were imploded with an ^{6}Li sample and five with an ^{7}Li sample. Two targets were imploded with no sample to record the incident neutron source spectrum. A preliminary comparison of the (n,2n) spectra from ^{6}Li and ^{7}Li in the 4- to 6-MeV range shows the expected enhancement in the ^{6}Li signal, as shown in Fig. 3. However, the predicted resonance for ^{7}Li at $E_x \sim 10.4$ MeV (a scattered neutron energy of ~3 MeV) was not apparent in the spectrum, suggesting that the state is either below the detection threshold (i.e., the cross section is below 10 millibarns) or the scattering resonance line width is too narrow to be resolved with the current diagnostic setup. The rich data set will be further analyzed in the coming weeks.
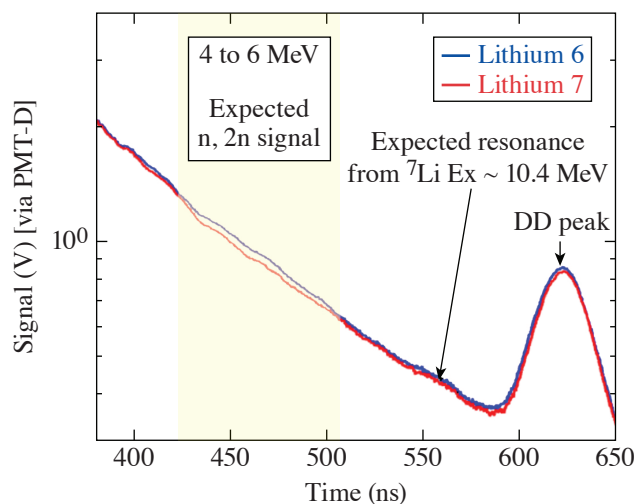
Figure 3
The double-differential cross section has been measured using a high-yield 14-MeV neutron source incident on $^{6(7)}$Li. A preliminary comparison of the (n,2n) spectra from ^{6}Li and ^{7}Li in the 4- to 6-MeV range shows the expected enhancement in the ^{6}Li signal.

E30004JR

Radiography Development for the Landau–Darrieus Instability

Principal Investigators: S. F. Kahn (LLNL)

Co-investigators: D. A. Martinez and V. A. Smalyuk (LLNL); and T. Goudal, G. Perez, L. P. Masse, L. Ceurvorst, and A. Casner (CELIA, University of Bordeaux, France)

The Landau–Darrieus Instability (LDI)[9] is an instability inherent to mediums undergoing combustion. Our experiments on OMEGA EP and the National Ignition Facility (NIF) aim to observe LDI with laser ablation[10] for the first time. The experi-

ments' laser intensity is too low (1.25 TW/cm^2) to reduce Rayleigh–Taylor instability growth. On OMEGA EP, we are attempting to observe perturbation growth early in time (up to 10 ns). Additionally, we will measure the shock-/ablation-front velocities. To develop our experiments on the NIF where we will observe LDI at later stages (>30 ns), we will test two backlighter choices (molybdenum and tantalum) that will optimize our radiography intensity and contrast.

In the experiments, we drive 100-mg/cm^3 foams made of carbonized resorcinol formaldehyde (CRF), with a 10-ns-long UV laser and radiograph from both the face and side of the target (see Fig. 4). The foam targets have machined oscillations with 100- and 50-μm wavelengths (see Fig. 5). The face radiograph is intended to measure the instability growth of those preimposed ripples. As the amplitude of the ripples grow, the optical depth will correspondingly increase. For the side radiographs, we oriented the target so that the ripples are along the diagnostic line of sight. In this way, the ripple growth could also be observed from the side if aligned. Additionally, using a time-gated detector, we can generate the shock-/ablation-front velocities. The 2-D shape of the front would be curved since the beam spot is smaller than the target face.
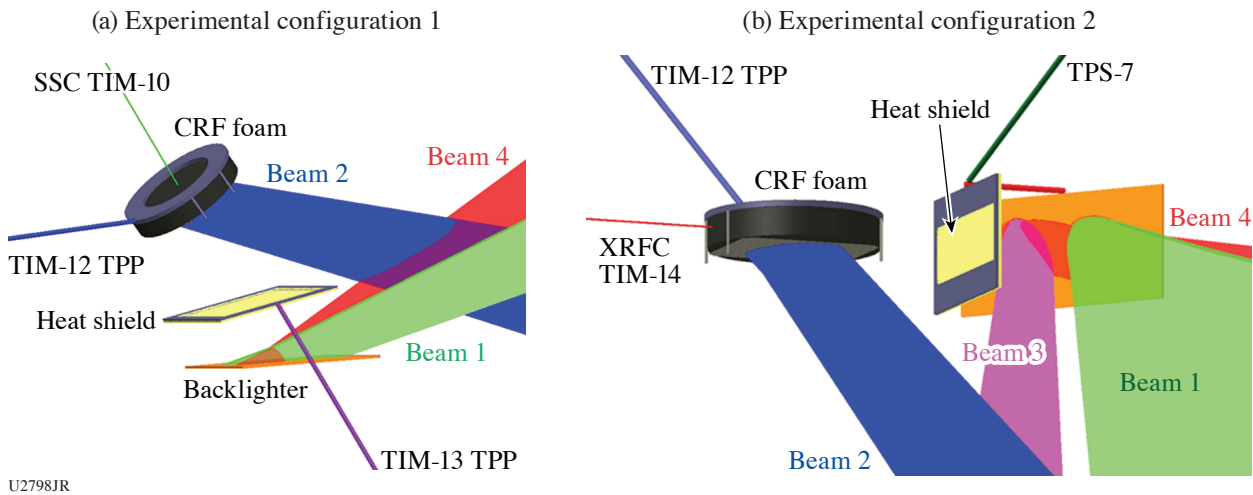

Figure 4

Two configurations were used. (a) The face-on configuration that used an Mo or Ta backlighter activated using two beams with a long-duration picketed pulse. One-dimensional radiographs are recorded onto an x-ray streak camera. A heat shield protects the foam from low-energy radiation from the backlighters. (b) Configuration 2 radiographs the target from the side using a vanadium backlighter onto an x-ray framing camera (XRFC). SCC: Sydor streak camera; TIM: ten-inch manipulator; TPP: two-photon polymerization; TPS: Target Positioning System.
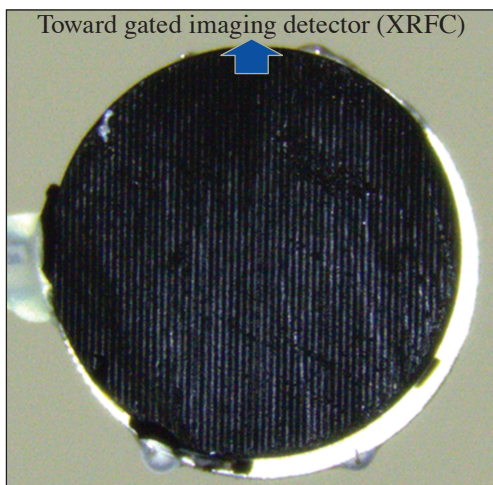

Figure 5

Photograph of one of the CRF foam targets with 100-μm-wavelength machined oscillations. The 6-mm-diam, 0.5-mm-thick target is oriented so that the ripples are along the imaging diagnostic line of sight.

Data from the streak camera (Configuration 1) did not show the expected results (see Fig. 6). We did not observe a discernable contrast across the ripples (horizontal direction). We saw oscillations in the time direction that are much lower frequency than the oscillations observed in the measured laser pulse. The current hypothesis is that the target and streak camera orientation was not aligned so that the 1-D image was smeared.

Excellent data was obtained, however, from the gated imager (Configuration 2), as shown in Fig. 7. Here, there are four time snaps staring at 3.5-ns and 2-ns intervals (drive duration is 0 to 10 ns). The ablation front is curved since the laser beam intensity decreases within the area of the target. The velocity of the shock was measured as ~18 μm/ns and matches the simulations to within 5 μm/ns. In the middle frames, it appears that ripple oscillations are visible in a few of the machined ripples. When we perform this experiment on the NIF, we will optimize to see this (increase magnification and radiograph contrast).
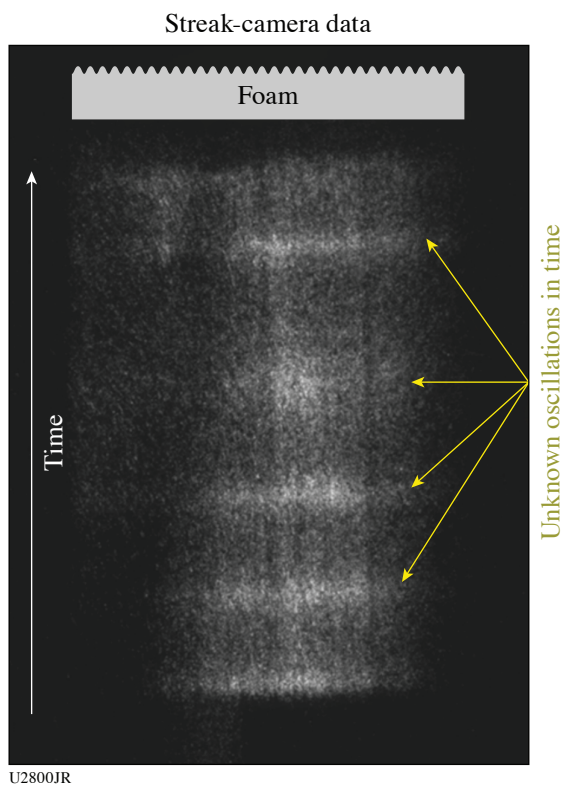

Figure 6

Data (shot 34687) from the SSC. Time goes in the vertical direction, while space is in the horizontal direction. The orientation and size of the expected ripple pattern are shown at the top of the image. The expected oscillations for the ripple pattern are missing. The bright horizontal lines are oscillations in time with an unknown origin. The vertical features are variations in the streak cameras photocathode sensitivity as these variations are seen in several shots at exactly the same location.
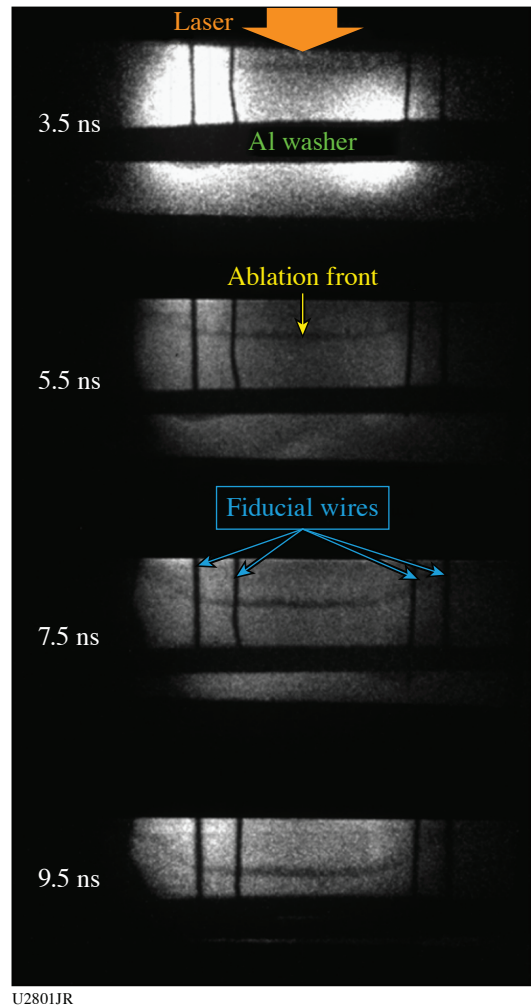

Figure 7

Data (shot 34692) from the Sydor framing camera. There are four time strips with the first strip on top at 3.5 ns and the other three strips recording at 2-ns intervals with 400-ps time gating. In the images, the laser irradiates the target from above. We use four wires as fiducials to set the space scale. The ablation front is the curved darker region that appears mostly across the images. It moves away from the laser as time increases at ~18 μm/ns.

Finally, we determined that the molybdenum backlighter was superior compared to the tantalum backlighter for x rays (2 to 3 keV). The signal from Mo was about 5× brighter and produced lower-energy x rays as desired for better contrast.

These experiments helped us to determine the course and configuration for our upcoming NIF experiments. The shock-velocity measurement validated our simulations. The trouble we saw with the streak camera influenced our decision to use a gated 2-D imager in our NIF experiments along with a molybdenum backlighter.

Proton Radiography of a Hybrid Laser Wakefield Accelerator Driven by a Kilojoule, Picosecond-Class Laser

Principal Investigators: N. Lemos, R. Simpson, P. King, and F. Albert (LLNL); and J. L. Shaw (LLE)

This work aimed to characterize the field's structure and time evolution of a hybrid laser wakefield accelerator (H-LWFA) driven by a kilojoule, picosecond-class laser using proton radiography. We measured for the first time the field's structure at the end of the interaction, i.e., at the plasma vacuum boundary. We observed the generation of large azimuthal magnetic fields that were confirmed by our quasi-3-D particle-in-cell simulations.

When the laser crosses the plasma–vacuum boundary, it leaves behind the blow-out region that is positively charged with a narrow central filament of ions and electrons.[11,12] When the electron bunch gets to the plasma–vacuum boundary, the most-energetic electrons escape the plasma, setting up a plasma potential barrier. This in turn confines the lower-energy electrons. As these electrons are pulled back into the plasma (return current), they form a vortex with an accompanying magnetic field that can reach tens of megagauss in magnitude. By Faraday's law, this magnetic field in turn produces a longitudinal electric field that will accelerate ions. This slowly varying longitudinal accelerating electric field can reach tens of GV/m. In this case, the B field has a defocusing effect that is negligible compared to the focusing force generated by the electric field. In this manner, the ion filament is maintained until the magnetic field decays over time. Typically, LWFA's are driven with low-energy (a few joules), femtosecond laser pulses and produce a small amount of accelerated charge (~1 nC). Here, using a kilojoule-class laser, we have already shown[13] that we can produce electron beams with hundreds on nC that will reinforce the vortex fields, making this the perfect platform to study this acceleration mechanism.

Due to its characteristics and the unique geometry of two orthogonal high-energy short pulses, OMEGA EP offers the perfect setup to perform a pump–probe experiment. We drove the H-LWFA with one beam and with the orthogonal beam generated a proton beam, through target normal sheath acceleration, that probed the H-LWFA. As it crosses the H-LWFA, the proton beam will be deflected by the magnetic and electric fields, creating a unique radiographic pattern on the proton detector (Fig. 8). Since

(a) 55 J, 10^{19} cm^{-3} (b) 110 J, 10^{19} cm^{-3} (c) 110 J, 2.5×10^{18} cm^{-3}
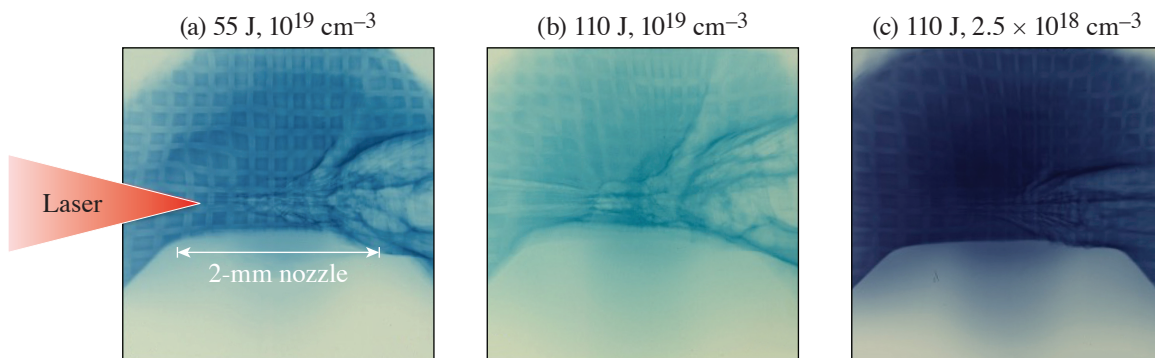
U2802JR

Figure 8
Proton radiography images 10 ps after the H-LWFA was formed.

different proton energies probe the H-LWFA at different times due to the different time of flight of each proton energy, it was also possible to record the time evolution of these fields on a single shot. Plasma density and laser energy scans were performed (Fig. 8), where it was possible to identify that the magnitude and spatial dimensions of the magnetic fields increased with plasma density and laser energy.

Investigating Giant Impacts Between Rocky Planets with Shock Equation-of-State Measurements on Natural Silicates
Principal Investigator: M. Millot (LLNL)
Co-investigators: D. E. Fratanduono (LLNL); and B. A. Chidester (University of California, Davis)

The Earth and other rocky planets likely formed after a series of energetic collisions in the early solar system. Simulations of these impacts rely on accurate equations of state and phase diagrams of natural materials to determine the amount of melting, vaporization, and mixing that occurs in the aftermath of a giant impact. Combined with data collected at the Sandia Z Machine, this study is the first to measure the principal pressure–density–temperature (P–ρ–T) Hugoniot of Fe-bearing orthopyroxene [bronzite, $(Mg_{0.9},Fe_{0.1})SiO_3$] to conditions relevant to giant impacts. To complement this data, we extended the experimental Hugoniot of Fe-free enstatite ($MgSiO_3$) to 1700 GPa, over twice the previously reported pressure. Additionally, we collected shock data for bronzite and olivine [$(Mg_{0.9},Fe_{0.1})_2SiO_4$] at lower pressures to constrain the onset of melting for these materials.

We completed ten shots on OMEGA EP in the one-day allocation, using alternating beams to increase the shot rate. Those data are combined with data collected in a previous shot allocation (FY19,20-SilicateEOS). As shown in Fig. 9, the enstatite compression curve from OMEGA EP closely matches data from the Z machine (this study), several previous experimental studies,[14,15] and molecular-dynamics (MD) calculations.[16] On the other hand, the bronzite compression curve diverges from the enstatite calculations, suggesting that even a small amount of Fe can affect the shock compressibility of silicate materials. All of these data, along with the melting curve information, will be incorporated into analytical equations of state for use in planetary impact simulations.
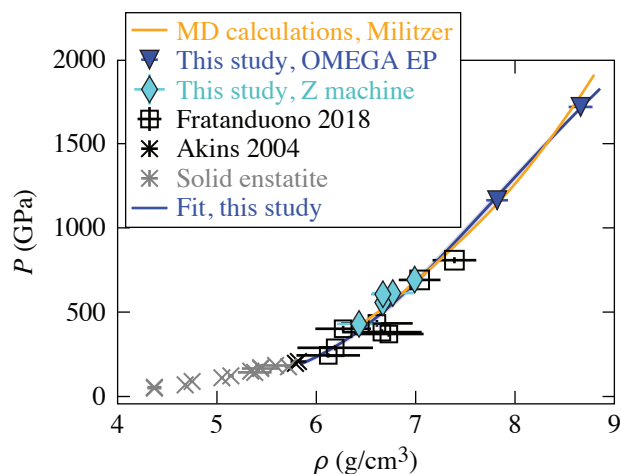

Figure 9
Preliminary P–ρ data for Fe-free enstatite (light gray symbols) and Fe-bearing bronzite (blue triangles). The enstatite data match *ab initio* estimates well, while the bronzite data diverge from these estimates at high pressure.

U2793JR

S *Factor for H(T,^{4}He)γ at Low Center-of-Mass Energies*
Principal Investigators: Z. L. Mohamed and J. P. Knauer (LLE); Y. H. Kim, H. Geppert-Kleinrath, and K. D. Meaney (LANL); and M. S. Rubery and A. B. Zylstra (LLNL)

While deuterium–tritium and deuterium–deuterium fusion are the most commonly studied fusion reactions due to their high cross sections, several lower-cross-section reactions are of interest to the fusion community as well as the nuclear physics and astrophysics communities due to their relevance to big-bang nucleosynthesis. Even though several such reactions have been studied

in accelerator experiments, ICF facilities offer a unique opportunity to study these reactions in a plasma environment that can directly produce astrophysically relevant temperatures, pressures, and electron screening effects that beam-based accelerator experiments cannot. This particular experiment focused on the $H(T,{}^4He)\gamma$ reaction, which produced a 19.8-MeV gamma. In addition to its relevance to big-bang nucleosynthesis, the $H(T,{}^4He)\gamma$ reaction is also of interest to the ICF community due to its use in mix experiments.

The goal of this experiment was to measure gamma rays on several HT implosions at different ion temperatures to determine an S factor for this reaction as a function of center-of-mass (CM) energy. The S factor is generally used to represent the rate of fusion reactions as they occur in high-density astrophysical environments and is considered to isolate the nuclear component of the cross section such that

$$S\big(E_{CM}\big) = \frac{E_{CM}}{\exp\left(-\dfrac{2\pi Z_1 Z_2 \alpha e^2}{\hbar v}\right)}\sigma\big(E_{CM}\big), \tag{1}$$

where E_{CM} is the CM energy, σ is the cross section, Z_1 and Z_2 are the atomic numbers of the interacting nuclei, α is the fine structure constant, e is the charge of an electron, $\hbar$ is the reduced Planck constant, and v is the relative velocity between the two nuclei. As HT-filled targets contain a small amount of D as contamination in the T part of the fill, D–T reactions also occurred in these "HT" experiments. The D–T neutrons from the $D(T,{}^4He)n$ reaction could therefore be used to measure a D–T neutron yield and ion temperature. The S factor for $D(T,{}^4He)n$ is considered to be well-known to within a few percent,[17] so the S factor for $H(T,{}^4He)\gamma$ can be calculated in relation to the $D(T,{}^4He)n$ reaction such that

$$S_{HT\gamma} = S_{DTn}\frac{Y_{HT\gamma}}{Y_{DTn}}\left[\frac{n_D A_{HT}\xi_{DT}^2 \exp(-3\xi_{DT})}{n_H A_{DT}\xi_{HT}^2 \exp(-3\xi_{HT})}\right], \tag{2}$$

where $Y_{HT\gamma}$ and Y_{DTn} represent gamma and neutron yields, A_{HT} and A_{DT} represent the reduced mass numbers for the HT and DT reactions, and ξ_{HT} and ξ_{DT} are functions of Z_1, Z_2, reduced mass number, and ion temperature.[18]

The experiment included six HT targets at various fill pressures and shot with various laser configurations as well as six analogous H_2 targets that were used to investigate the contribution of any non-nuclear background. Cherenkov detectors including the Atomic Weapons Establishment diagnostic for areal density (DAD) and the LANL gas Cherenkov detectors (GCD-1 and GCD-3) were used to measure gammas. The DAD uses a quartz radiator, which can detect gammas down to 0.4 MeV. GCD-1 and GCD-3 both used CO_2 at different pressures for gamma energy thresholds of 6.3 and 12 MeV, respectively. No non-nuclear background was observed on any of these detectors; however, the GCD-3 signals showed unexpected oscillations that were thought to be associated with the photomultiplier tube, while the DAD measurement was thought to be contaminated by gammas from the remaining glass shell due to its very low threshold. The GCD-1 data were therefore considered to be the most reliable for use in the S factor analysis.

Because the total gamma signal in these implosions includes gammas from both $H(T,{}^4He)\gamma$ and $D(T,{}^5He)\gamma$ in similar amounts, the $D(T,{}^5He)\gamma$ component must be subtracted from the total signal to isolate the HT gamma. The DT γ signal area per D–T neutron as measured by GCD-1 in Ref. 19 was used to perform this subtraction along with neutron yields as measured by nTOF detector 12mntofN. Ion temperatures were also measured from 12mntofN. Shots of similar ion temperature were grouped together and considered to represent a single data point with an average ion temperature and gamma yield.

The final data set used to calculate the S factor included average ion temperatures of 4.6, 9.0, and 12.7 keV, which correspond to CM energies of 16, 25, and 32 keV. The inferred S factors at these CM energies were 2.9 ± 0.6, 3.4 ± 0.6, and 4.4 ± 0.9 eV*barn as calculated using the GCD-1 gamma signal, DT neutron yields as measured by 12mntofN, and reference D–T neutron S factor from Ref. 17. The error bars on these measurements include uncertainties on the number of Cherenkov photons generated in the

detector as calculated using Geant4 simulations performed by collaborator M. S. Rubery. At present, the only accelerator data available for comparison are that from Ref. 20, which include two data points at CM energies of 12.3 and 31.2 keV as well as a fit to these two data points and accelerator data collected at higher energies. Figure 10 shows the data points and best-fit line from Ref. 20 plotted along with the data points from the OMEGA measurement. The OMEGA data points appear to be 25% to 70% higher than the best-fit line from Ref. 20; however, they appear to be in approximate agreement with the two individual accelerator data points from Ref. 20 within their error bars. Overall, further investigation of the $H(T,^4He)\gamma$ reaction seems to be warranted considering the lack of accelerator data for comparison at these low CM energies.
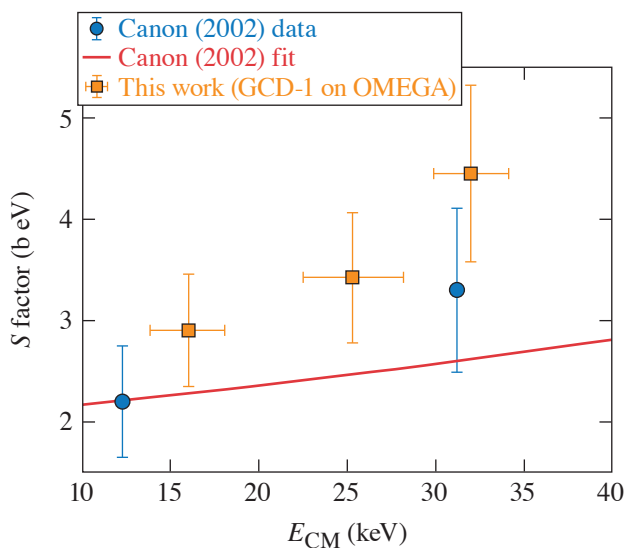
Figure 10

Comparison between GCD-1 data points from this work (yellow) and data points from Ref. 20. These two data points were the only accelerator data points available at these low CM energies. Reference 20 also provides a best-fit line to these data points and accelerator data at much higher energies (red line). The mean values of the GCD-1 data points appear to be 25%–75% higher than the best-fit line provided by Ref. 20; however, they appear to be in agreement with the two individual data points from Ref. 20 within their error bars.

E29997JR

Atomic Physics at Petapascal Pressures

Principal Investigators: P. M. Nilson, S. X. Hu, D. T. Bishel, and D. A. Chin (LLE); and S. B. Hansen (SNL)

Under HED conditions, the building blocks of matter (atoms) experience tremendous pressures, ranging from millions to many trillions of atmospheres (1 million atm = 1 Mbar = 10^{11} Pa; 1 PPa = 10 Gbar). Understanding how atomic physics may be altered in these conditions is fundamentally important to the exploration of stellar interiors and brown/white dwarfs, planetary cores, and ICF implosions. The LBS campaign (PetapascalAtmPhys-21A) was successfully carried out on 18 February 2021 and used our recently developed platform for implosion spectroscopy on OMEGA. In this campaign, we used Cu-doped CH capsules with a 30-μm-thick shell, which are filled with 20 atm of D_2 gas and 1% Ar by atomic fraction [see Fig. 11(a)]. These targets were imploded by 60 OMEGA laser beams with a 1-ns square pulse, having a total laser energy of ~27 kJ on target. When the imploding shell stagnates, a hot spot is formed, which "backlights" the compressed Cu-doped CH shell (ρ = 10 to 20 g/cm^3, kT = 50 to 500 eV). Both time-resolved and time-integrated x-ray spectra are recorded by high-resolution spectrometers. A typical time-resolved spectrum is shown in Fig. 11(b), in which both the K_α line emission and 1s–2p absorption of Cu are presented. In FY21, we developed the density functional theory (DFT)-based kinetic modeling code *VERITAS* to self-consistently understand these experimental measurements. A preliminary comparison of time-integrated experimental data (solid red line) with *VERITAS* (solid blue line) and traditional collision-radiative-equilibrium (CRE) model predictions (dashed green line) is illustrated in Fig. 11(b). It is shown that the traditional CRE models failed to reproduce the pronounced 1s–2p absorption feature that is observed in the experiment, while the DFT-based *VERITAS* modeling gives an overall good account of the 1s–2p absorption in Cu (although some minor detailed discrepancies exist). *VERITAS* modeling reveals that the dominant 1s–2p absorption was caused by the 2p level
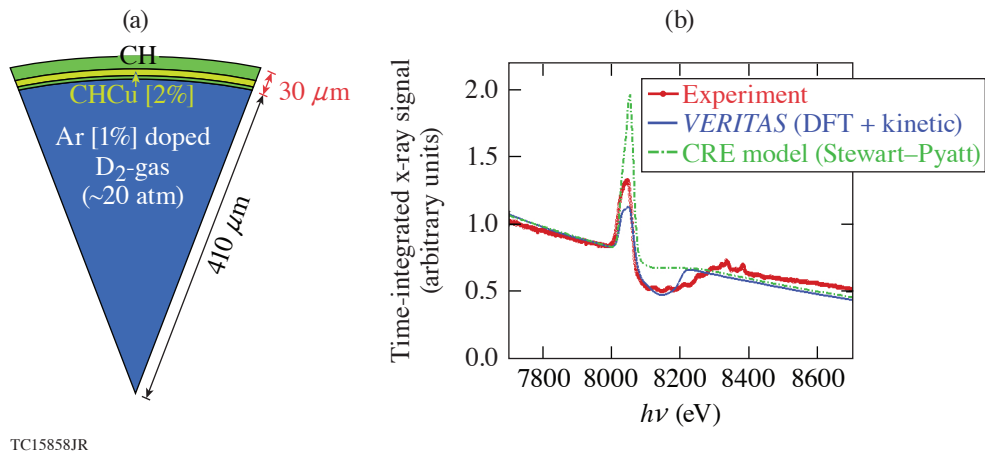
(a)

(b)

TC15858JR

Figure 11

(a) Schematic of the implosion target that was used in these experiments, which includes a buried Cu-doped plastic layer inside the shell and a D_2 Ar (1 at. %)-filled core. (b) An example comparison of a measured time-integrated x-ray spectrum with *VERITAS* and CRE model predictions.

depletion of Cu due to heating of the CHCu layer by a thermal wave originating from the hot implosion core. This comparison highlights the necessity for a self-consistent treatment of atomic ionization in these dense plasma conditions. A quantitative comparison of time-resolved spectra with *VERITAS* model predictions is underway, and a manuscript reporting these findings is in preparation.

Comparison and Validation of Dynamic Magnetic-Field Diagnostics on Laser-Driven Coils and MIFEDS
Principal Investigators: J. L. Peebles, J. R. Davies, D. Barnak, R. B. Spielman, and R. Betti (LLE)

The initial objectives of the LBS shot day were as follows: (1) compare diagnostic responses between laser-driven coils (LDC's) and the known fields of the magneto-inertial fusion electrical discharge system (MIFEDS) and a separate fast rise pulser; (2) fully map (in 3-D) the electric and magnetic fields for a laser-driven coil at different times during the driving laser interaction; and (3) compare the measurements collected by B-dot probing, Faraday rotation, and proton radiography.

All the campaign objectives were met with a single shot day and two additional shots afforded by the facility during short-pulse/long-pulse timing qualification. These two additional shots allowed us to demonstrate the axial proton radiography technique using the known 40-T central field of a MIFEDS coil. The axial radiography technique utilizes weaker radial fields to cause a rotation effect in the proton radiograph proportional to the square root of the proton energy. There were some doubts about the technique since in the paraxial approximation no rotation should be seen (since the radial field changes sign on either side of the coil). With these shots, however, we demonstrate that in reality a significant rotation can be measured and scales exactly as expected with proton energy. These shots also helped to verify the proton spectrum, where the first two films in Fig. 12 contain mainly shadows of 9-MeV protons that were primarily deposited on the third film. Two shots were conducted in this configuration, the second of which reversed the field, which reversed the rotation direction of the radiograph. The axial probe was then applied to laser-driven coils, along with a simultaneous transverse probe. These measurements demonstrated that double-plate, "capacitor"-style, laser-driven coils developed very weak fields, with currents of the order of 2.5 kA (Fig. 13). The single-plate coil styled in a helical pattern showed slightly larger currents at around 15 kA close to the driven plate and 5 kA further away.

For these experiments a new diagnostic platform was developed called the Mini B-dot probe. While B-dots are nothing new in terms of technology for time-resolved measurements of magnetic fields, we wanted to develop our own platform that could be customized and calibrated for use on OMEGA EP. These B-dots were calibrated using the 1-kA, high-repetition-rate pulser shown in Fig. 14, which demonstrated their sensitivity to low-mode dc perturbations. In the experiments, the B-dot probes could distinguish the two laser pulses [long pulse (LP) driving the LDC, short pulse (SP) for creating protons] and showed an order-of-

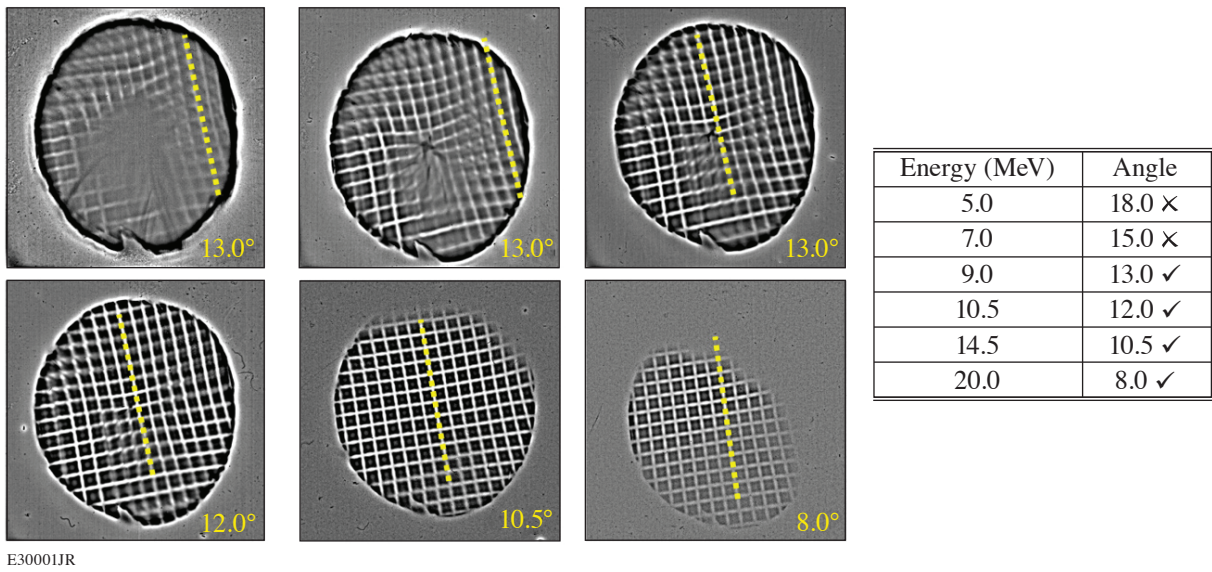| Energy (MeV)	Angle
5.0	18.0 ✗
7.0	15.0 ✗
9.0	13.0 ✓
10.5	12.0 ✓
14.5	10.5 ✓
20.0	8.0 ✓

E30001JR

Figure 12
Axial proton radiography data taken from a MIFEDS reference shot. Protons passing through the coil receive an azimuthal kick as they pass the radial magnetic field. They travel on this altered trajectory until they receive an opposing kick from the field upon leaving the coil, resulting in a net spatial rotation in the radiograph related to the time of flight (and therefore energy) of the proton.
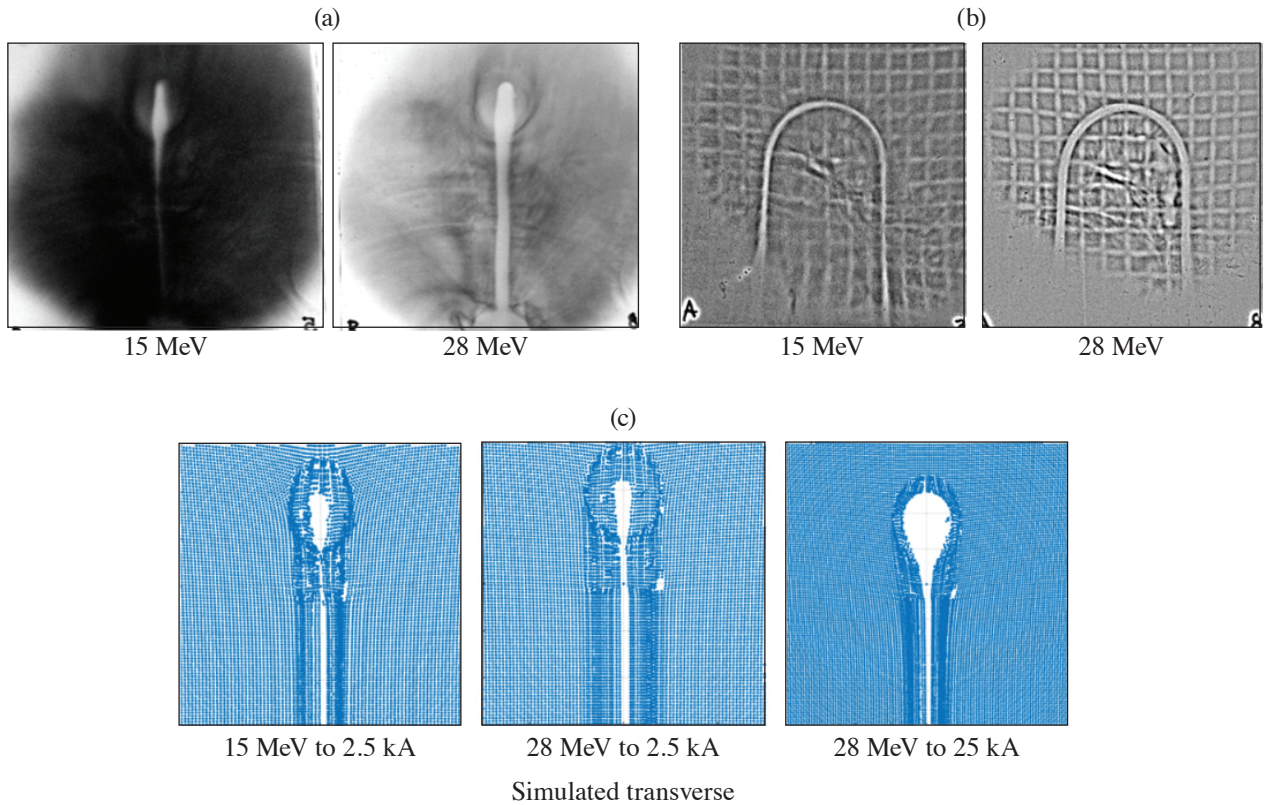

E30002JR

Figure 13
Transverse, axial, and simulated radiography data of double-plate LDC targets. Transverse radiographs are very sensitive to small currents and are required to reach 2.5 kA of current in the LDC. The current is too small to create any sort of resolvable rotation in the axial probe compared to the MIFEDS test shot. As an example, 25 kA of current creates voids far larger on the transverse radiograph than were measured, indicating no presence of a strong magnetic field.
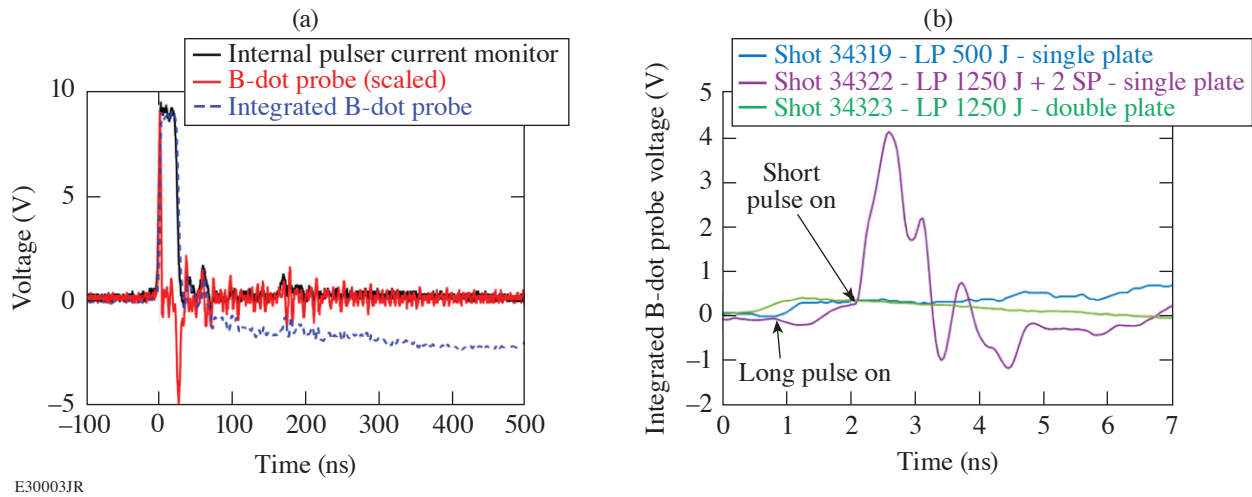
Figure 14

(a) Calibration data from the B-dot probe mathematically integrated and compared against the internal pulser current measurement. During the current pulse there is near-perfect agreement, although on longer time scales a dc offset causes significant error in the integrated measurement. (b) During experimental measurements, the long pulse and short pulse were offset by 1 ns, with additional delays due to signal time of flight between laser incidence locations. If assumed to be from magnetic field only, the long-pulse signal corresponded to an upper limit of 50 kA of current and the short pulse roughly 500 kA (an unphysical value by energy conservation).

magnitude-larger signal when the SP was active. By energy conservation we can understand that the signal on the B-dot probe from the short pulse was not from the magnetic field. This tells us that the B-dot probe measurement provides an upper limit on magnetic-field measurements since it is unable to discriminate between magnetic and electric fields. This also suggests that previous experiments that produced very high field measurements using a B-dot probe may have had their results skewed by short-pulse interactions in the experiment.

Measurements of Warm-Dense-Matter Silicon Based on Angularly and Spectrally Dispersed X-Ray Scattering
Principal Investigators: H. Poole and G. Gregori (Department of Physics, University of Oxford); M. K. Ginnane, D. N. Polsin, S. X. Hu, S. P. Regan, and J. R. Rygg (LLE); and T. White (University of Nevada, Reno)

To improve the modeling of WDM silicon, we investigated the plasma conditions seen at 1.1-Mbar compression using active shock breakout (ASBO), angularly resolved x-ray diffraction, and spectrally resolved inelastic x-ray Thomson scattering (XRTS) on the OMEGA EP Laser. Current experimental data[21–23] have led to contradictory conclusions regarding the best model for predicting ionization potential depression.

The total dynamic structure factor is given by[24]

$$S(k,\omega) = \left| f(k) + q(k) \right|^2 S_{ii}(k,\omega) + Z_f S_{ee}^0(k,\omega) + Z_b \int \tilde{S}_{ce}(k,\omega - \omega') S_S(k,\omega') d\omega',$$

where $S_{ii}(k,\omega) \sim S_{ii}(k)\delta(\omega)$ is the ion–ion dynamic structure factor and Z_b and Z_f are the number of bound and free electrons, respectively. In the investigated XRTS scattering regime, the noncollective, unknown terms are $S_{ii}(k)$, $q(k)$, and Z_f. Angularly resolved x-ray diffraction provides, in mid- to high-Z materials, a direct measurement of $\left| f(k), q(k) \right|^2 S_{ii}(k) \sim Z_b^2$, which therefore leaves XRTS sensitive only to the ionization state, Z_f.

The experimental design used a variant of the PXRDIP platform on OMEGA EP, which allowed for simultaneous characterization of the compressed Si sample using ASBO, PXRDIP, and XRTS, using the ZSPEC diagnostic. The investigated pressure was 1.1 Mbar, with x-ray scattering recorded at 70° and 97°.

As shown in Fig. 15, current analysis of the relative elastic scattering peaks across the two angles collected on this shot day, alongside a 95° shot from a previous campaign date, indicates a relative S_{ii} ratio between the lower and higher scattering angles. It should be noted that the second 70° shot (yellow curve) is omitted from the analysis. This is because, as seen in Fig. 15(a) and in the legend, $\Delta t = -1.23$ ns, the x rays scattered while silicon was still partially in the solid state. In Fig. 15(d), the accepted XRTS shots were fed into a Monte Carlo Markov Chain[25] (MCMC) analysis code that produces a range of accepted S_{ii} fits and posterior parameter distributions (shown in Fig. 16) based on the experimental data. To produce these fits, the 70° is normalized to 1, and the 95° and 97° points are restrained to within some ratio band as shown in Fig. 15(d).
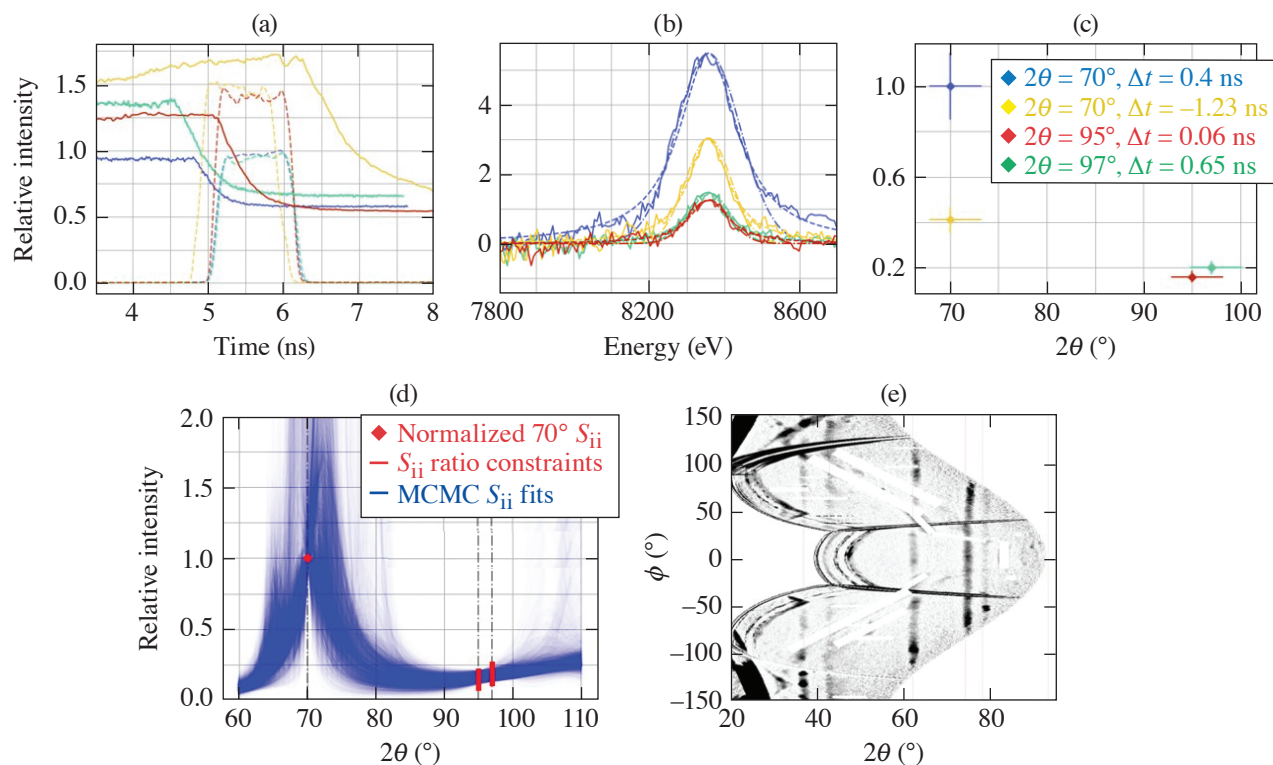

U2794JR

Figure 15
(a) Solid curves: profile of shock breakout determined from active shock breakout (ASBO) analysis. Dashed curves: relative intensity of the laser profiles incident on Cu x-ray backlighter. The time between shock breakout and the x-ray source is indicated in the legend. (b) X-ray Thomson scattering (XRTS) profiles from varied scattering angles. The elastic scattering peaks have been fit with Gaussian and Lorentzian curves shown as dashed and dashed–dotted lines, respectively. (c) Area of elastic scattering against scattering angle. The area error is determined as the difference between Gaussian and Lorentzian fits seen in (b). (d) Attempt at S_{ii} Monte Carlo Markov Chain (MCMC) fitting. (e) Powder x-ray diffraction image plate (PXRDIP) analysis isolating the Ag pinhole diffraction lines.

The current parameter distributions from this MCMC analysis is indicated in Table III. Information has been obtained on the mass density and silicon ionization, but the electron temperature remains broadly distributed. These results need to be compared to accurate simulations. Additionally, further constraints could be applied to these conditions as a result of further PXRDIP analysis.

Table III: MCMC parameter distributions for predicted Si mass density and ionization. The normal distributions are visualized in Fig. 16.

Parameter	MCMC analysis
Mass density (g/cm^3)	2.0±0.2
Ionization	6±2
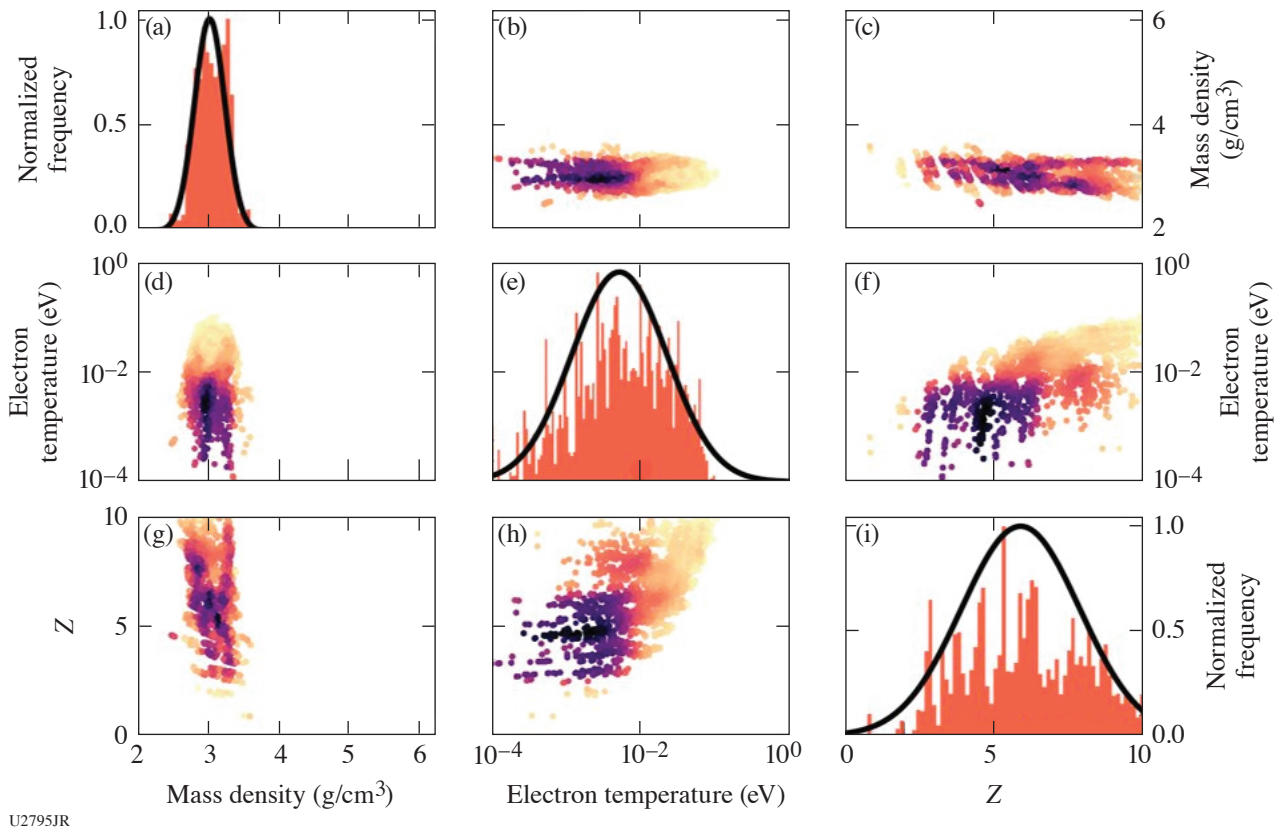
Figure 16

MCMC analysis for S_{ii} data obtained from elastic XRTS peaks shown in Fig. 15(c). The upper and lower quadrants show the density maps for the relation between the different fitted plasma parameters. The central plots are the normalized parameter histograms with normal distributions fitted over them.

Measurement of the ^{3}H(n,2n)^{2}H Breakup Cross Section Using Direct-Drive Inertial Confinement Fusion Implosions

Principal Investigators: H. G. Rinderknecht and C. J. Forrest (LLE); and M. Gatu Johnson (MIT)

Nuclear reactions involving small numbers of nucleons are of great interest to modern nuclear physics theory because they constrain low-energy reactions important to nuclear astrophysics. Low-energy light-ion reactions challenge the current capabilities of nuclear physics simulations in a regime where full-physics simulations are plausible. ICF implosions have been used to measure the differential cross section for low-energy light-ion reactions including elastic scattering of deuterons and tritons by 14.1-MeV D–T fusion neutrons,[26] six-nucleon fusion reactions,[27] and the deuteron breakup reaction D(n,2n)p (Ref. 28). However, almost no published data exist for the triton three-body breakup reaction T(n,2n)D, and what data exist are of extremely poor quality.[29] The relatively low cross section of this reaction (~50 mb) has made it difficult to assess in implosions not specifically designed to measure this process.
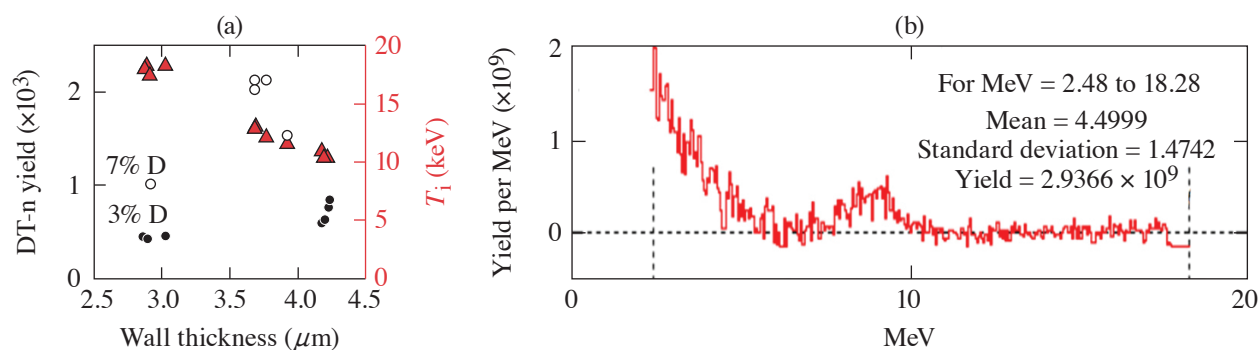
We performed a series of direct-drive implosion experiments using the OMEGA laser to measure the first high-quality deuteron spectra from the triton-breakup reaction. Targets were filled with tritium-rich fuel $\left[f_T = n_T / (n_T + n_D) = 93\% \text{ or } 97\% \right]$ designed to balance the requirement of a high yield of D–T fusion neutrons and a low background of elastically scattered deuterons. The implosions were SiO$_2$ spheres with 3-μm or 4-μm walls and 1070-μm outer diameter. These were predicted to generate moderate areal density ($\rho R = 5$ to 10 mg/cm^2) in symmetric implosions, limiting deuteron energy loss on the way out of the fuel. The

U2795JR

targets were imploded with 0.6-ns and 0.9-ns square pulses, respectively, to match the predicted bang time and reduce the effect of capsule charging on the charged-particle spectra. Neutron yields of 0.4 to 2.1×10^{13} were observed, as shown in Table IV and plotted in Fig. 17. The primary diagnostic was the magnetic recoil spectrometer (MRS) used in charged-particle mode to record deuteron spectra, which was expected to observe between 2 and 9×10^3 deuterons per shot. Secondary diagnostics included the charged-particle spectrometer (CPS2) to measure elastically scattered (n,t) tritons.

Analysis of the CPS2 diagnostic shows elastically scattered triton spectra that are consistent in magnitude and spectral shape with implosion areal density of the order of 1 to 10 mg/cm^2, as shown in Fig. 17. Both deuteron and triton signals were observed in the MRS data. Interpretation of the data has been more difficult than anticipated due to the co-location of substantial (n,t) triton and D–T fusion α backgrounds with the (n,d) and t(n,2n)t signals of interest. The alpha, triton, and deuteron signals are separable in principle since different particle species produce different track diameters in the CR-39 detection medium; however, this work

Table IV: Experimental design and results from the TBreak-20A Campaign. Two wall thicknesses (3.0 and 4.0 μm) and two fuel D:T ratios (7% and 3% deuterium) resulted in four implosion types. Neutron yields in the range 4 to 21×10^{12} were observed, resulting in a predicted 2 to 9×10^3 triton-breakup deuterons observed by the MRS in each implosion.

Shot number	RID	Pulse shape	Wall (μm)	Deuterium %	Y_{DTn} (10^{12})	$\langle T_i \rangle$ keV	$Y_{T(n,2n)D}$ (10^8)	*$N_{detected}$T(n,2n)D
98789	79825	SG06v001	3.0	7%	10.1	17.5	7.3	5210
98790	79953				4.5	18.1	3.3	2250
98791	79956	SG06v001	3.0	3%	4.3	18.4	3.2	2160
98792	79957				4.6	18.4	3.4	2290
98794	79297				15.3	11.7	10.2	6490
98795	79958	SG09v002	4.0	7%	21.3	13.0	14.2	9040
98796	79959				21.3	12.2	14.2	9040
98797	79960				20.3	13.2	13.5	8610
98799	79954				6.0	11.1	4.0	2690
98800	79962	SG06v001	3.0	3%	7.6	10.5	5.1	3410
98802	79963				6.4	10.5	4.3	3410
98803	79964				8.4	10.5	5.6	3750

E30010JR

Figure 17

(a) Observed D–T fusion neutron yield (black) and burn-averaged ion temperature (red) from the Tbreak-20A Campaign. Fuel mixtures with 3% deuterium and 7% deuterium are shown as filled and open circles, respectively. (b) Elastically scattered triton spectrum measured by CPS2 on shot 98794. The spectral shape and yield are consistent with an areal density in the range of 1 to 10 mg/cm^2.

is ongoing. We anticipate that we will be able to precisely infer areal density using the MRS (n,t) triton spectra. We will then use the differing spectral shape of the (n,d) and t(n,2n)d deuteron spectra on each shot to infer what fraction of the deuterons is produced from triton breakup and use this value to constrain the cross section of the t(n,2n)d breakup process.

Proton Radiography of Target Normal Sheath Acceleration Fields in the Long-Pulse Regime
Principal Investigators: R. Simpson, N. Lemos, D. Mariscal, E. Grace, G. Scott, J. Kim, and T. Ma (LLNL); and J. L. Shaw (LLE)

In this experimental campaign we performed a time-dependent radiograph of the surface fields (front and back) of a laser-irradiated solid target while varying the laser pulse length. The goal was to investigate the increased coupling and higher-energy target normal sheath acceleration (TNSA) proton that have been reported when using picosecond laser pulse durations (low and high intensity)[30] as opposed to when using tens of femtosecond laser pulses.

In the TNSA mechanism, a high-power laser is incident upon the front side of a thin (~μm scale) solid target where electrons are efficiently heated to high energies. These heated electrons traverse through the target and set up a sheath field on the back side, which accelerates ions from the rear surface (Fig. 18). This sheath field is generated by the electron pressure gradient and has accelerated ions up to ~100 MeV (Ref. 31). Both short-pulse beamlines of OMEGA EP were used to simultaneously create and probe the TNSA fields. A thin Cu foil was driven by one laser beam, creating the TNSA fields at the back of the target. A second laser beam irradiating a thin gold foil generated a proton beam that probed the TNSA fields generated by the first laser pulse. Different proton energies probed the TNSA fields at different times due to the different time of flight of each proton, so it was possible to record the time evolution of these fields on a single shot (Fig. 18). A parameter scan over several pulse durations (keeping the laser intensity constant) showed that the maximum proton energy was achieved for a laser pulse duration >10 ps. Figure 18 shows the time evolution of a Cu foil expanding from 0 to 50 ps for a laser pulse duration of 0.6 ps. At longer pulse
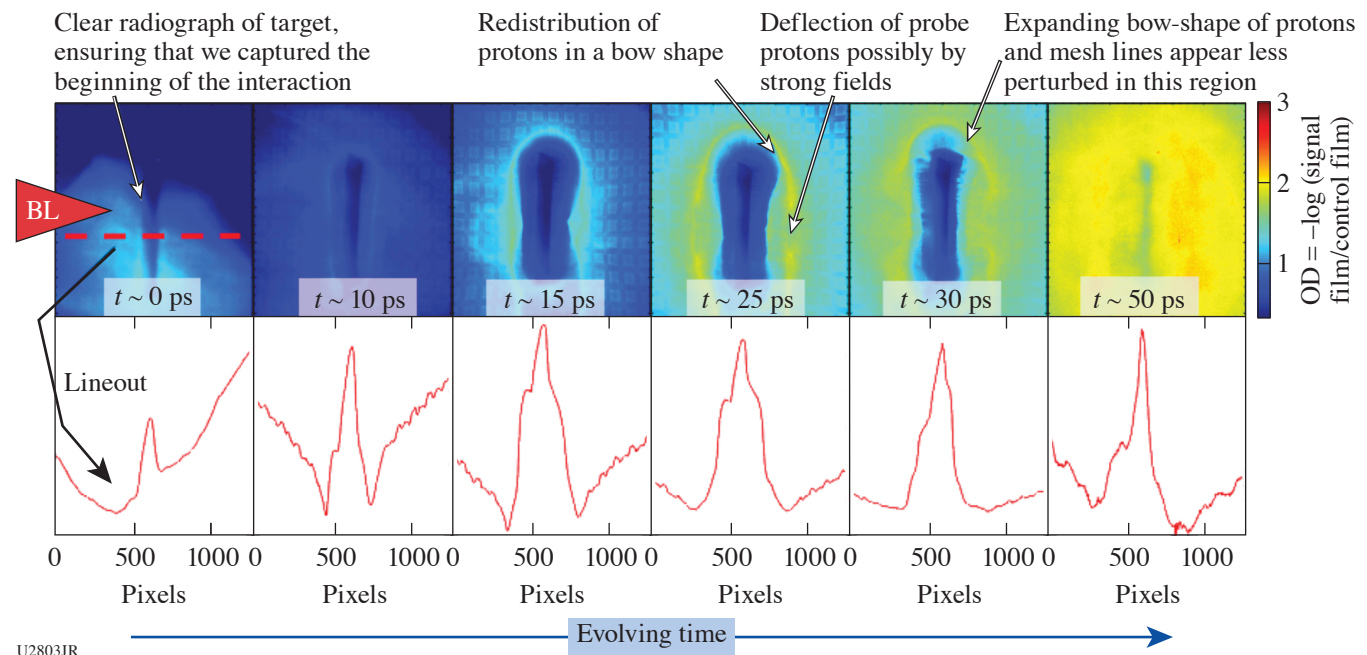

Figure 18
Single-shot proton radiography of an expanding Cu foil irradiated by a 0.6-ps, 34-J laser pulse. The top row images show the radiochromic film signal from 0 to 50 ps. The bottom row shows the horizontal lineouts at the center of the Cu foil.

lengths, which are most relevant to our work on the NIF-ARC (Advanced Radiographic Capability Laser), we missed time = 0 (when laser pulse one irradiates the Cu foil). We will extend this work beyond these preliminary shots to capture these dynamics in the multipicosecond regime.

Determination of High-Pressure Phase Transformation Mechanisms at the Atomic Scale
Principal Investigators: S. Singh, R. F. Smith, J. H. Eggert, and J. McNaney (LLNL); and J. Wicks (Johns Hopkins University)

For many materials, the application of pressure results in an atomic rearrangement into a lower-energy crystal structure that is accompanied by an associated volume collapse. Such phase transformations are commonplace in nature and can fundamentally alter the transport, chemical, and mechanical characteristics of a solid. Reconstructive phase transformations—which is a type of transformation in which no group–subgroup relationship between the parent and transformed phase exists—constitutes an important class of such phase transitions. Determining the sequence of atomic movements that facilitate pressure-induced phase transformations has been a great challenge in the field of high-pressure physics, toward the goal of developing predictive time-dependent and mechanistic atomic-pathway–dependent models. Despite decades of research, these processes remain poorly defined and largely restricted to theoretical study.[32–35]

We designed a series of shock-compression shots to explore the melt curve of FeO and texture evolution in SiC. The pressure was tuned by changing the laser power, and samples were probed just before shock breakout using x-ray diffraction. Figure 19(a) shows the target pressure states for the FeO sample.[36] Several experimentally measured phase boundaries, as well as the theoretically predicted melt curve, are also shown.

By using a multilayered target package, we were able to obtain high-quality diffraction data between 200 and 360 GPa. Examples of raw and integrated data are shown in Fig. 19(b). VISAR (velocity interferometer for any reflector) was employed as
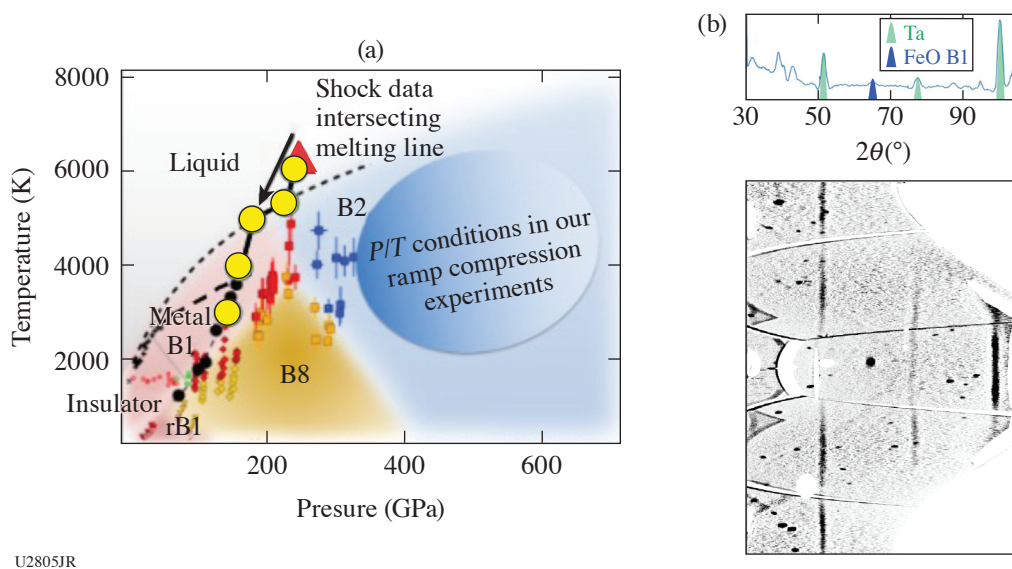

U2805JR

Figure 19

(a) The phase diagram of FeO with theoretically predicted phase boundaries and data from previous studies is shown. Target pressures proposed during the campaign are shown with the yellow circles. (b) The diffraction data corresponding to the red triangle (~230 GPa). Raw (lower) and integrated (upper) data from the FeO target package are shown. The powder lines are from the W pinhole. There is diffraction recorded from the B1 phase, which is well above the theoretically calculated melt curve on the FeO Hugoniot.

a secondary diagnostic in the campaign to allow pressure determination. Over one shot day, we took 11 shots and successfully characterized the structural behavior of FeO and SiC at several different pressure and temperature states. Crystalline diffraction from the FeO B1 phase was observed at pressures well above the theoretical melt curve and presents an interesting avenue for future experiments.

OMEGA EP NuclTNSA Campaign
Principal Investigator: C. Stoeckl (LLE)

The 26 January LBS campaign on OMEGA EP aimed to characterize the TNSA deuteron beam emitted from 25-μm-thick titanium targets exposed to 1 atm of D_2 at 350°C for 24 h. The OMEGA EP laser with intensities between 1 and 7×10^{17} W/cm^2 was directed onto these targets, and the profile and energy spectrum of the emitted deuteron beam was measured using radiochromic film (RCF) and Thomson parabola ion energy (TPIE).[37] In separate experiments, the deuteron beam was directed onto deuterated polyethylene (CD) targets to induce D–D fusion and test the feasibility of this platform for nuclear reaction studies. The existing nTOF detectors at 90° and 130° were employed to detect any D–D fusion neutrons.

Insights from these experiments are utilized to produce tritiated titanium targets, which have been demonstrated to emit a comparable tritium beam when irradiated by OMEGA EP. This platform is currently the only one worldwide to deliver a multi-MeV triton beam for nuclear experiments.

1. Deuteron Beam Characteristics

This campaign featured for the first time a step absorber for TPIE to remove the heavy C^{n+} and O^{n+} contaminants in the deuteron beam. Aluminum foils of thicknesses between 10 and 100 μm were arranged in bands directly in front of the image plate, with the thicker foils in regions where higher ion energies are expected. The results are shown in Fig. 20(a), where the left panel demonstrates that even an untreated Ti target produces various lines associated with surface contaminants. These can be removed from the beam with the step filter, as shown in the center, such that the deuterated target on the right produces only D^+ and H^+ lines.

The corresponding deuteron spectra for several energies are shown in Fig. 20(b). In general, the spectra have an exponential shape with cutoff energies around 10 MeV. It is evident that the deuteron beam spectrum can be controlled coarsely by increasing
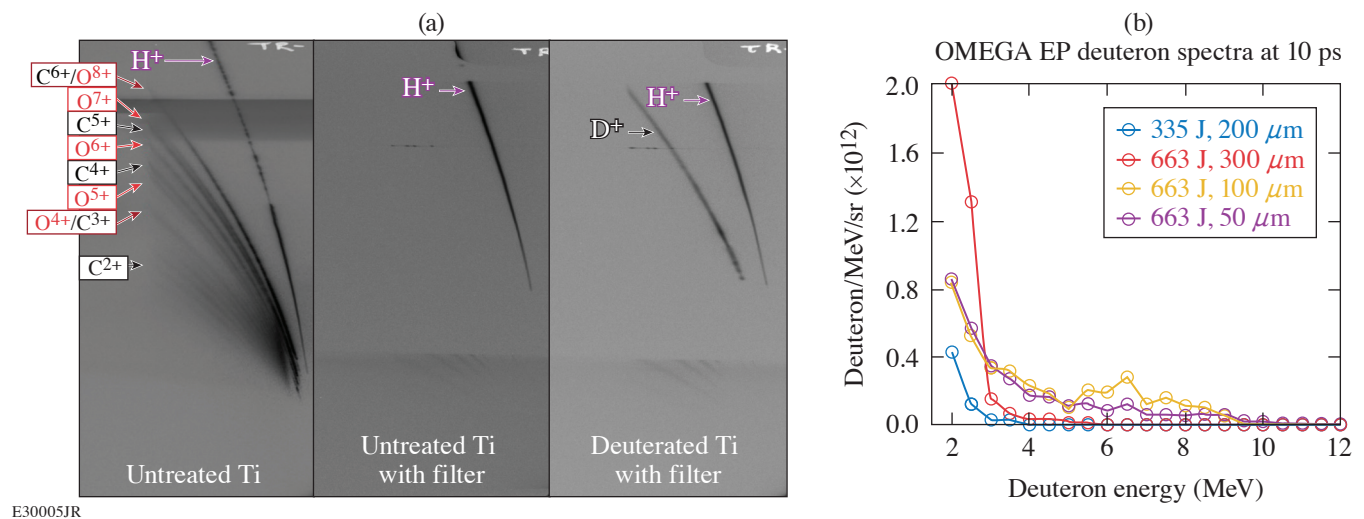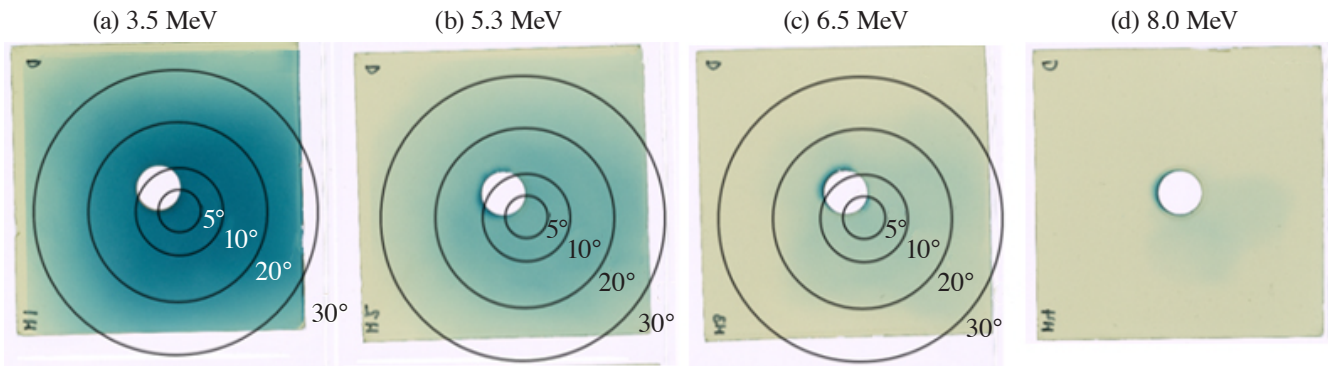

Figure 20
(a) Raw TPIE image plates with and without the described filter. (b) Corresponding deuteron spectra.

(a) 3.5 MeV (b) 5.3 MeV (c) 6.5 MeV (d) 8.0 MeV

E30006JR

Figure 21
Raw RCF images. High-energy ions tend to be closer to the beam axis.

the laser energy, which increases the deuteron cutoff energies and total yields at all energies. Prior experiments with CD targets[38] suggested that further beam shaping is possible with additional laser beams, which will be examined in a planned campaign.

The RCF measurement delivered a spatial beam profile consistent with expectations from other TNSA experiments.[38,39] Figure 21 shows that the low-energy ions tend to be emitted at angles of up to 30°, whereas the high-energy ions tend to stay close to the center.

2. Pilot Nuclear Experiment
The described deuteron beam was directed onto a secondary CD target 5 mm behind the first, and two nTOF detectors were employed to look for any D–D fusion neutrons. The neutron spectra, corrected for instrument responses and attenuation effects and calibrated against ICF experiments, are shown in Fig. 22. Two peaks at 2.5 MeV (90°) and 2.7 MeV (130°) are evident, which is consistent with kinematically shifted D–D fusion neutrons.

(a)
90°

(b)
130°
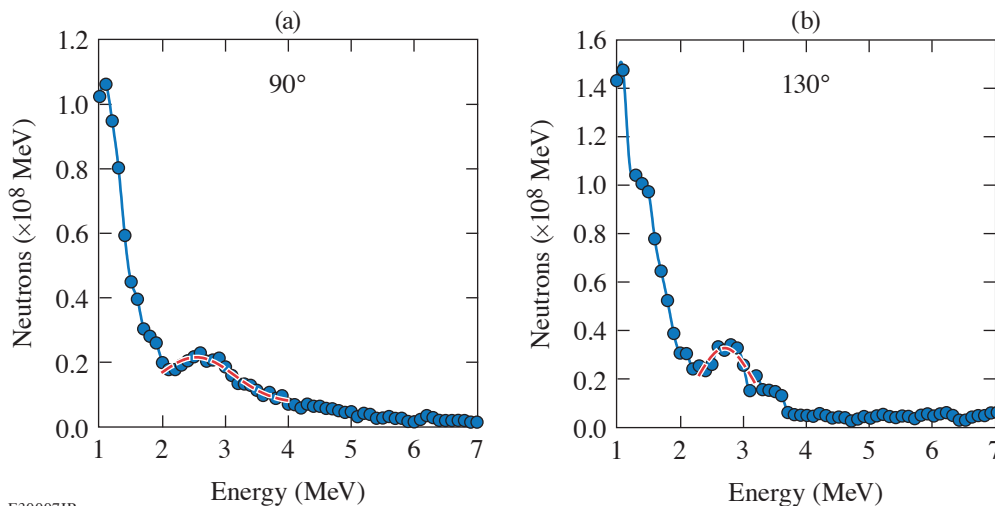
E30007JR

Figure 22
Neutron time-of-flight spectra at two different angles, featuring a small D–D fusion peak.

Prior campaigns[38] suggested that the signal-to-background ratio can be improved by enclosing the primary target in a plastic cylinder that shields the target chamber from high-energy protons. The neutrons produced by the associated (p, n) reactions with the chamber walls increase the background substantially. A follow-up campaign is planned to investigate this hypothesis and improve the neutron signals from these experiments.

Report for H$_2$-H$_2$O-DAC-21A

Principal Investigator: G. Tabak (LLE)

Co-investigators: G. W. Collins and J. R. Rygg (LLE); and R. Dias (University of Rochester)

The purpose of this campaign was to study hydrogen-rich systems with planetary science applications in mind. Both hydrogen and water are major components of ice giant interiors, and a recent work predicts that at extreme pressures an H$_3$O structure will form, which would have implications for planetary interior modeling.[40] While hydrogen and water are immiscible at ambient conditions, it is known that they can mix in certain ratios at ~1 GPa and higher pressures, a range accessible by the diamond-anvil cell (DAC) platform, which is now standard at the Omega Laser Facility.[41] This experiment required several new developments for the team, including a new liquid–gas filling technique as well as reaching 3 to 5 GPa, which is a higher pressure range than what had been achieved in previous experiments with these cells. The filled DAC's would then be shock-compressed on OMEGA 60 and taken to the several-100-GPa range. VISAR and a streaked optical pyrometer (SOP) is used to directly measure the shock velocity, reflectivity, and self-emission. Impedance matching with a quartz standard is used to measure the pressure and density, while the self-emission is referenced to quartz to infer the shock temperature, giving a full equation of state. The evolution of pressure, density, temperature, and reflectivity along the Hugoniot would then be explored for potential signatures of phase changes and novel chemistry at extreme conditions.

Unfortunately, after this proposal was submitted, the gas loader unexpectedly broke down and repairs were completed a week before the shot day. It was impossible to fully develop the new techniques as originally planned, so the cells were filled with pure methane (CH$_4$), which contributed to an ongoing effort to understand this material. CH$_4$ is another hydrogen-rich system that is also a major constituent of giant planets and is, therefore, closely related to the original goal. It is predicted to have an intricate phase diagram at pressures of several 100 GPa, including eventual separation into diamond and hydrogen, and elucidating the properties of methane at these extreme conditions would provide internal insight into the ice layer of giant planets such as Uranus and Neptune.[42] After some improvements to the target preparation process, methane DAC's were prepared with pressures reaching 4 to 5 GPa, which is the pressure range that was desired for the hydrogen–water mixture.

High-quality data on methane were obtained at the challenging precompression of 4 to 5 GPa, bringing the experimental conditions closer to planetary interior conditions. While the 100- to 400-GPa range is easy to reach with shocks, high precompres-
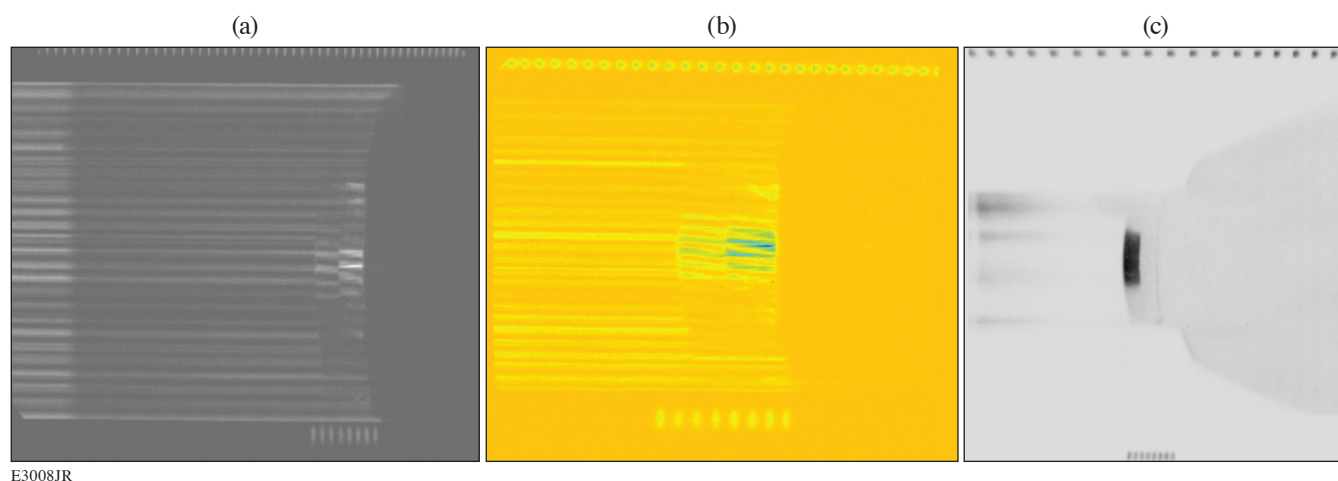

(a) (b) (c)

E3008JR

Figure 23

(a) VISAR1, (b) VISAR2, and (c) SOP data for shot 101060. The two fringe events at the spatial center of the target, co-timed with the eight-comb, indicate shock breakout into quartz and methane. The self-emission of the quartz standard is clearly seen as the dark rectangular region on the SOP, and the methane self-emission occurs afterward on the image.

sion is necessary to lower the temperature of the shock state and bring it closer to the pressure–temperature conditions believed to exist inside planets. Therefore, these results constitute a significant enhancement of the data set on precompressed methane. Figure 23 shows a representative VISAR and SOP datum from one of the shots.

To summarize, while it was impossible to follow through with the original plan, the team demonstrated significant improvements with the DAC platform and obtained important data on methane, a closely related material, which will give new insight into planetary interiors.

X-Ray Phase-Contrast Imaging of Imploding Strong Shock Waves

Principal Investigators: W. Theobald, J. J. Ruby, and D. Cao, (LLE); L. Antonelli, M. Khan and N. Woolsey (York Plasma Institute, Department of Physics, University of York, UK); F. Barbato, V. Bouffetier, L. Ceurvorst, and A. Casner (CELIA, University of Bordeaux, France); and R. H. H. Scott (Central Laser Facility, STFC Rutherford Appleton Laboratory, UK)

The goal of this LBS joint shot day campaign was to demonstrate 2-D x-ray phase-contrast imaging (XPCI) of a converging strong shock wave in a spherical solid CH target using a short-pulse laser-driven backlighter source. The application of XPCI to diagnose laser-induced shock waves proved to be powerful in determining the shock-front position in both the high- and low-density regions of the target.[43] Due to the high sensitivity to density variations, XPCI is the ideal tool to detect the position of a shock front, especially in the case when it is propagating in a low-density region, in the presence of multiple shocks, detecting asymmetries in the shock front, and studying hydrodynamic instabilities such as the Rayleigh–Taylor and the Richtmyer–Meshkov instabilities. In a previous experiment, the XPCI technique was successfully demonstrated in planar target geometry on OMEGA EP by applying a short-pulse backlighter source to measure the density profile of a strong shock wave in a cylindrical CH target.[44] High-quality radiographs were obtained that clearly showed the phase-contrast enhancement at the shock front using a wire source target, providing a spatial resolution of 14 ± 2 μm in the horizontal direction and 18 ± 2 μm in the vertical direction. The next step was to apply the developed XPCI platform to spherical implosions on OMEGA and to provide 2-D snapshot XPCI radiographs of a converging shock wave in a solid CH sphere with a short-pulse laser-driven backlighter source.

The experimental setup is shown in Fig. 24(a). The 60 OMEGA UV (λ = 351 mm) laser beams were focused on a CH sphere with a diameter of 1.05 mm using SG5-650 distributed phase plates, distributed polarization rotators, smoothing by spectral dispersion modulation, and a 1-ns square pulse. One of the two IR short-pulse beams from the OMEGA EP laser was focused onto a backlighter target that consisted of a Cu wire with a diameter of 10 μm glued onto a 10-μm-thick CH substrate with an area
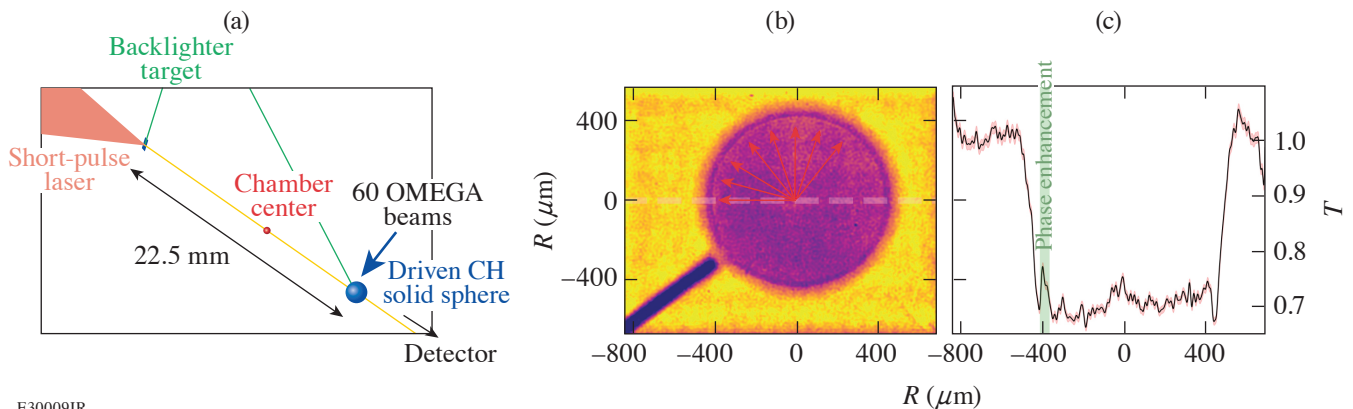
E30009JR

Figure 24

(a) Experimental setup and (b) sample measured radiograph of shot 99189 that was taken at a probing time of 6.5 ns after the start of the 1-ns drive pulse showing phase-contrast enhancement at the shock front. The CH sphere was imploded by the 60 OMEGA beams with a total energy of 640 J and an intensity of 2×10^{13} W/cm^2. The dark diagonal strip at the lower left is the shadow of the target stalk. The red arrows in the sphere indicate the parts of the shock front that present phase enhancement. (c) Transmission lineout along the dashed horizontal line. The pink area indicates the experimental error. The signal excursion at the transmission minimum is caused by phase-contrast enhancement.

of $300 \times 300\ \mu m^2$. The IR beam with 100-ps pulse duration was focused with an intensity in the range of 2×10^{16} W/cm^2 to 1×10^{17} W/cm^2 with normal incidence onto the target with the wire aligned along the radiography axis pointing to a passive imaging plate (IP) detector plate placed in a heavy metal shielded box. The backlighter produced a strong emission between 8 and 9 keV, predominately from the He$_\alpha$ and Ly$_\alpha$ resonance lines. The distance from the backlighter to the CH sphere was 2.2 cm and the distance from the CH sphere to the IP detector was 1.3 m, providing a spatial magnification of 60×. A 23-μm-thick Cu foil and a 254-μm-thick polyethylene terephthalate (PET) blast shield were placed in front of the detector, which provided a transmission of ~40% for the 8-keV backlighter radiation and strongly attenuated the x-ray emission for photon energies below 5 keV from the corona of the driven target.

We obtained radiographs of an imploding shock wave at different probing times by shifting the timing between the drive and the backlighter beams. Significant hard x-ray emission in the backlighter emission produced a strong background, which reduced the image contrast. In addition, the x-ray emission from the plasma of the driven target contributed to the background especially at high drive laser energies. Reducing the backlighter energy and the drive laser energy improved the image contrast, which made it possible to record radiographs of the imploding spherical shock wave at various times. The radiographs are of poorer image quality than the ones obtained in the previous experiment on OMEGA EP under similar experimental conditions. Phase-contrast enhancement was observed in the radiographs although with reduced quality. An example image is shown in Fig. 24 together with an inferred transmission lineout. The phase enhancement is not uniform and visible in some parts of the spherical implosion. This could be due to the nonperfect alignment of the source or an azimuthal variation in the shock strength. A backlighter-only shot with a static Au grid provided an *in-situ* measurement of the spatial resolution, which provided 22±3 μm, worse than in the OMEGA EP planar target experiment. This could explain the lower amount of observed phase enhancement in the spherical target experiment.

The image-plate detector usage is restricted to low drive energies (<1 kJ) because of the background x-ray emission from the plasma of the driven CH sphere. Higher drive energies require a time-gated detector. An attempt was made to use a time-resolved detector (two-strip time-gated x-ray imager) instead of the IP. This was partially successful. A time-gated radiography of the shock wave driven by a shaped laser pulse and 15 kJ of drive laser energy was obtained; however, the detector was not well aligned and significant hard x-ray emission from the backlighter produced a strong inhomogeneous background. Part of the imploding shock wave was observed on the bottom strip and the shadow of the target stalk on the upper strip. Lowering the short-pulse laser intensity helps to reduce this background, but it also diminishes the amount of useful Cu He$_\alpha$ emission at ~8.4 keV that radiographs the object. Further optimization of the spherical target platform is required by optimizing the signal-to-background ratio and the detector.

Retrieving Density Profiles of Ion Species with Talbot–Lau Interferometry
Principal Investigators: T. E. Weber (LANL); M. P. Valdivia (Johns Hopkins University); V. Bouffetier, G. Perez-Callejo, L. Cervoust and A. Casner (CELIA); and G. Kagan (Imperial College London)

In recent years, multispecies physics has been attracting an increasing amount of attention in the high-energy-density physics context. For example, a number of experiments indicate that in laser-driven spherical implosions of DT and D^{3}He plasmas, the relative concentration of the D and T ions can change, thereby degrading the yield. Another area where the multispecies effects can be of paramount importance is the physics of hohlraums. As the high-power lasers irradiate the inner surface of a hohlraum, the Au ions are ablated to create a high-Z plasma jet. This jet can then collide with another such jet or with a jet of different ions, resulting from the ablation of the outer surface of the fuel capsule.

Ideally, to understand the basic physics behind and implications of these effects, spatially resolved measurements of each species' densities would be needed. One could then validate directly the newly developed theoretical models for species separation and

interpenetration. One complication is that the relevant densities are often too high for standard diagnostics such as optical Thomson scattering. This project has attempted to understand spatial profiling of the relevant densities with a very novel diagnostic (the x-ray Talbot–Lau interferometer), which is currently being developed on OMEGA EP. The present version operates with 8-keV photon energy, which makes accessible electron densities of about 10^{23} cm^{-3}, therefore allowing one to study the conduction zone of the ablation layer.

The experiment parameters were as follows: A long-pulse laser (~150 to 900 J, 1 ns, ~10^{13} W/cm^2) was used to drive a thin 5-μm foil, resulting in plasma jets emerging from the front and rear surfaces. A short-pulse laser (90 to 150 J, 10 ps, ~10^{16} W/cm^2) was then used to drive a copper foil to produce an 8-keV probe beam for Talbot–Lau x-ray interferometry. Three basic types of driven foils were employed: plastic (CH), copper (Cu), and bronze (94% Cu/6% Sn). In principle, Talbot–Lau interferometry allows inference of an average atomic number that is directly related to the relative species concentration in a plasma with two ion species. Therefore, bronze targets were chosen based on attenuation and refraction signatures, which were expected to be the most pronounced for rather disparate species with the high-*Z* element being a minority.
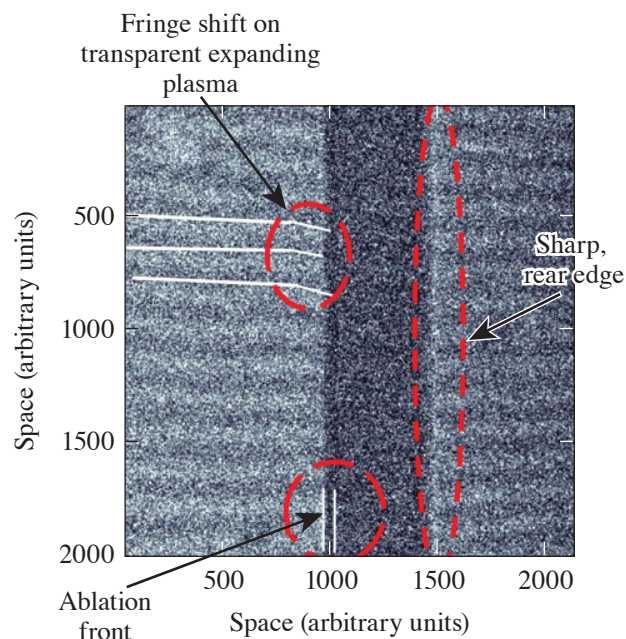
Figure 25
The raw data with enhanced contrast from CH shot 35242 showing promising features. The image dimensions are equivalent to 675 to 675 μm. Driving beam: 150 J, 1 ns, 700-μm spot size; backlighter: 150 J, 10 ps, 120-μm spot size, 0.5-ns delay with respect to the driving beam.

U2805JR

In the experiment, however, bronze (and pure copper) targets produced too much of the self-emission that overshadowed the 8-keV signal from the backlighter, dramatically reducing diagnostic signal-to-noise ratio, which was also observed when probing the plasma jets at later times. Therefore, CH targets were driven, and self-emission was then found to be much lower with the plasma densities extending all the way from solid to those transparent for 8-keV photons. Promising features were observed, as shown in Fig. 25. Talbot–Lau moiré fringe contrast is high enough to distinguish fringe shifts, indicating electron density gradients near the foil surface and making evident a strong high-density ablation front unresolvable by 8-keV illumination. While we are unlikely to be able to infer the individual species (i.e., the C and H) densities, inferring the total ion density profile may be possible. This alone would provide data to validate existing ablation models.

Extreme Deformation and Failure of High-Entropy Alloys by Laser Shock-Induced Compression and Tension
Principal Investigators: S. Zhao (LBNL)
Co-investigators: Q. Yu and C. Stan (LLNL)

High-entropy alloys (HEA's) are a class of metallic alloys containing three or more elements in significant atomic proportion. They exhibit generally high yield strength and fracture toughness and are good candidates for engineering applications such as

the aerospace industry. This project was initially interested in (1) the spall strength behavior of these materials, and (2) the 2-D velocity anisotropy through the HEA grain structure. Due to catastrophic failure of the OMEGA high-resolution velocimeter (OHRV) system, we were able to focus only on the first part of the LBS request.

We studied the spall strength of several HEA's and steels to several tens of GPa. The experimental setup (Fig. 26) consists of three individual targets that are independently shot, one of which was a spall velocimetry target and two of which were recovery tube spall targets.
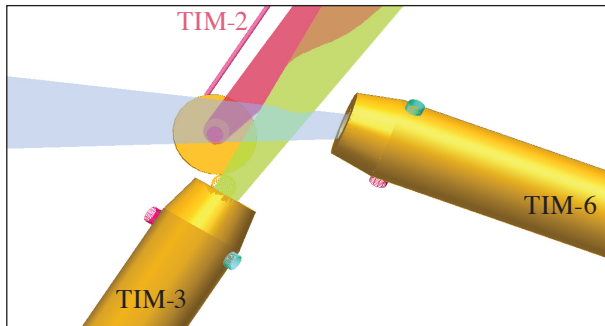
Figure 26
Schematic diagram of the experimental setup. Two recovery tubes are mounted in TIM-3 and TIM-6. A VISAR target is mounted from TIM-2 and positioned such that the back of the target points toward TIM-5, where the ASBO is located. Each target is driven with a square laser pulse shape and one to two drive beams, depending on the desired shock strength, and the beams were defocused to ~3 mm in order to cover the entire sample surface. Since the materials do not have established shock behavior, energy was scaled between 100 and 500 J in order to cover a range of possible pressure.

U2806JR

During our one shot day, we were able to execute a total of nine shots. On the first half-day, we found that the VISAR targets had been mounted backward, causing a severe lack of reflectivity in the VISAR instrument. On the second half-day, we were target limited, due to the last-minute redesign of the experiment as a result of the OHRV failure. We collected three good VISAR data points and one data point where one VISAR leg malfunctioned. The recovery targets from both days remain to be analyzed as a result of a reduction in personnel at LBNL. Electron microscopy will be used to determine the grain behavior at the spall surface.

REFERENCES

1. M. Millot *et al.*, Nat. Phys. **14**, 297 (2018).

2. M. Millot *et al.*, Nature **569**, 251 (2019).

3. J. R. Rygg *et al.*, Rev. Sci. Instrum. **83**, 113904 (2012).

4. Y.-J. Kim *et al.*, Sci. Rep. **11**, 5610 (2021).

5. C. Wang *et al.*, Phys. Plasmas **22**, 102702 (2015).

6. C. H. Allen *et al.*, Appl. Opt. **61**, 1987 (2022).

7. *Report of the Workshop on High Energy Density Laboratory Physics Research Needs*, Office of Science, U.S. Department of Energy, Washington, DC (15–18 November 2009).

8. T. R. Boehly *et al.*, Opt. Commun. **133**, 495 (1997).

9. L. D. Landau, Zh. Eksp. Teor. Fiz. **14**, 240 (1944).

10. P. Clavin and L. Masse, Phys. Plasmas **11**, 690 (2004).

11. L. Willingale *et al.*, Phys. Rev. Lett. **96**, 245002 (2006).

12. N. Lemos *et al.*, J. Plasma Phys. **78**, 327 (2012).

13. J. L. Shaw *et al.*, Sci. Rep. **11**, 7498 (2021).

14. J. A. Akins *et al.*, Geophys. Res. Lett. **31** (2004).

15. D. E. Fratanduono *et al.*, Phys. Rev. B **97**, 214105 (2018).

16. B. Militzer, High Energy Density Phys. **9**, 152 (2013).

17. H. S. Bosch and G. M. Hale, Nucl. Fusion **32**, 611 (1992); **33**, 1919(E) (1993).

18. A. B. Zylstra *et al.*, Phys. Rev. C **101**, 042802(R) (2020).

19. Y. Kim *et al.*, Phys. Rev. C **85**, 061601 (2012).

20. R. S. Canon *et al.*, Phys. Rev. C **65**, 044008 (2002).

21. S. M. Vinko *et al.*, Nat. Commun. **6**, 6397 (2015).

22. D. J. Hoarty *et al.*, Phys. Rev. Lett. **110**, 265003 (2013).

23. D. Kraus *et al.*, Phys. Rev. E **94**, 011202(R) (2016).

24. J. Chihara, J. Phys.: Condens. Matter **12**, 231 (2000).

25. M. F. Kasim *et al.*, Phys. Plasmas **26**, 112706 (2019).

26. J. A. Frenje *et al.*, Phys. Rev. Lett. **107**, 122502 (2011).

27. D. T. Casey *et al.*, Phys. Rev. Lett. **109**, 025003 (2012).

28. C. J. Forrest *et al.*, Nucl. Instrum. Methods Phys. Res. A **888**, 169 (2018).

29. J. M. Kootsey, Nucl. Phys. A **113**, 65 (1968).

30. R. A. Simpson *et al.*, Phys. Plasmas **28**, 013108 (2021).

31. F. Wagner *et al.*, Phys. Rev. Lett. **116**, 205002 (2016).

32. S.-H. Guan and Z.-P. Liu, Phys. Chem. Chem. Phys. **18**, 4527 (2016).

33. K. Kadau *et al.*, Phys. Rev. Lett. **98**, 135701 (2007).

34. B. Dupé *et al.*, Phys. Rev. B **87**, 024103 (2013).

35. D. Zahn and S. Leoni, Phys. Rev. Lett. **92**, 250201 (2004).

36. F. Coppari *et al.*, Nat. Geosci. **14**, 121 (2021).

37. J. A. Cobble *et al.*, Rev. Sci. Instrum. **82**, 113504 (2011).

38. C. Stoeckl *et al.*, Nucl. Instrum. Methods Phys. Res. B **453**, 41 (2019).

39. E. L. Clark *et al.*, Phys. Rev. Lett. **85**, 1654 (2000).

40. P. Huang *et al.*, Proc. Nat. Acad. Sci. **117**, 5638 (2020).

41. W. L. Vos *et al.*, Phys. Rev. Lett. **71**, 3150 (1993).

42. B. L. Sherman *et al.*, Phys. Rev. B **86**, 224113 (2012).

43. L. Antonelli *et al.*, Europhys. Lett. **125**, 35002 (2019).

44. L. Antonelli *et al.*, "X-Ray Phase-Contrast Imaging of Strong Shocks on OMEGA EP," to be submitted to Review Scientific Instruments.